



UNIVERSITÀ  
DEGLI STUDI  
FIRENZE

DOTTORATO DI RICERCA IN FISICA E ASTRONOMIA  
CICLO XXV

COORDINATORE Prof. Livi Roberto

**The structure of the Broad Line Region  
and its effects on virial Black Hole masses**

Settore Scientifico Disciplinare FIS/05

**Dottorando**

Dott. Sirigu Mauro

**Tutore**

Prof. Marconi Alessandro

**Coordinatore** Prof. Livi Roberto

Anni 2010-2012



*Alla mia famiglia.*



# Contents

<b>1</b>	<b>Introduction</b>	<b>1</b>
1.1	Supermassive black holes in nearby galaxies . . . . .	4
1.2	SMBH-galaxy correlations . . . . .	9
1.3	AGN taxonomy . . . . .	12
1.3.1	Radio-quiet Nuclei . . . . .	13
1.3.2	Radio-loud Nuclei . . . . .	16
1.4	Evidences for a Unified Model of AGN structure . . . . .	17
1.5	SMBHs growth and AGN feedback . . . . .	22
1.6	BH mass ladder: BH masses in Active Galactic Nuclei . . . . .	23
1.6.1	Reverberation mapping (RM) . . . . .	24
1.6.2	Single epoch (SE) mass measurements . . . . .	26
1.7	Outline of the thesis . . . . .	28
<b>2</b>	<b>The physical origin of the radius-luminosity relation</b>	<b>30</b>
2.1	Introduction . . . . .	30
2.2	The Broad Line Region Model . . . . .	33
2.2.1	Single cloud photoionization models . . . . .	35
2.2.2	LOC - Locally Optimally-emitting Clouds . . . . .	39
2.2.3	CPE - Clouds in Pressure Equilibrium . . . . .	43
2.3	The radius-luminosity relation: model results . . . . .	45
2.3.1	“Dusty wall” models in the LOC framework . . . . .	46
2.3.2	“Dusty wall” models in the CPE framework . . . . .	54

2.3.3	The extended <i>dust free</i> models in the LOC framework . . . . .	57
2.3.4	Extended <i>dusty</i> models in the LOC framework . . . . .	58
2.3.5	Extended <i>dusty</i> models in the CPE framework . . . . .	61
2.4	The origin of the radius-luminosity relation . . . . .	68
2.4.1	Possible scenarios . . . . .	71
2.5	Line profiles and black hole mass measurements . . . . .	73
2.6	Conclusions . . . . .	76
<b>3</b>	<b>Spectral fitting of SDSS DR7 and DR10 Quasars</b>	<b>78</b>
3.1	Introduction . . . . .	78
3.2	AGN surveys . . . . .	80
3.2.1	Radio selection . . . . .	80
3.2.2	IR selection . . . . .	81
3.2.3	Optical and UV selection . . . . .	82
3.2.4	X-ray and high energy selection . . . . .	84
3.3	The Sloan Digital Sky Survey . . . . .	86
3.4	The DR7 and DR10 Quasar catalogues . . . . .	91
3.5	The state of the art in spectral fitting of quasar spectra . . . . .	92
3.6	A new machinery in quasar spectral fitting . . . . .	94
3.6.1	QSO selection . . . . .	95
3.6.2	Spectral fitting of DR10 quasars . . . . .	96
3.6.3	Results . . . . .	100
<b>4</b>	<b>The effect of radiation pressure on virial black hole masses</b>	<b>113</b>
4.1	Introduction . . . . .	113
4.2	Overview of the radiation pressure correction and of tests on its importance	115
4.3	Possible Observational Evidences for Radiation Pressure . . . . .	118
4.4	Calibration of $M_{\text{BH}}$ based on $H\beta$ . . . . .	120
4.5	Calibration of $M_{\text{BH}}$ based on Mg II and on C IV . . . . .	127
4.6	Line width vs continuum luminosity distributions: data . . . . .	131

---

4.7	Line width vs continuum luminosity distributions: model and observations .	132
4.7.1	Comparison of Mg II and $H\beta$ LV distribution . . . . .	136
4.7.2	Comparison of Mg II and C IV LV distributions . . . . .	137
4.8	A coherent physical picture . . . . .	142
4.9	Conclusions . . . . .	143
<b>5</b>	<b>General conclusions</b>	<b>146</b>
	<b>Bibliography</b>	<b>150</b>
	<b>Acknowledgements</b>	<b>167</b>



# Chapter 1

## Introduction

Most of modern astrophysics research is based on the effort of trying to answer one fundamental question: how the present universe could emerge from the almost perfectly homogeneous one traced by the cosmic microwave background and the large scale galaxy structure. While it is fundamental to understand which are the basic processes that led to the formation of the wide variety of galaxies and their stellar populations, it is also important to establish whether the different evolutionary scenarios have a common engine and, most importantly, how can we get observable evidences of such processes. Obviously, the constance of the speed of light offers an essential help in this quest, letting us to convert distances into the timeline of the history of the universe but, as it will soon be clear, the same importance has to be attributed to the development of sophisticated instruments and theoretical models that can allow us to understand the structure of small objects – if compared with the size of the galaxy which host them – and the light sources associated with them.

Recent simulations (Springel et al. 2005 and references therein) have shown how gravity can provide the right explanation of the formation of large scale structures and filaments. While the acceleration of the expansion of the Universe is driven by the dark energy component, contributing with  $\sim 70\%$  of the total energy density, the coalescence of barionic matter is guided by dark matter. These latter two components contribute respectively a  $\sim 4\%$  and a  $\sim 27\%$  of the total energy density, according to the cosmological standard model here adopted (Tegmark et al. 2004). These simulations are certainly a starting point in understanding the

overall framework, but do not explain most of the observed phenomenology.

The discovery of *active galaxies*, from Carl Seyfert's first detections on, certainly provided an important piece of the puzzle. Some spiral galaxies were indeed discovered to be characterized by an anomalous surface brightness radial distribution, with an extremely bright central light source emitting up to  $10^{44} \div 10^{45} \text{ erg s}^{-1}$  in the B band ( $M_B \sim -23$ ). These central regions were eventually hundreds of times brighter at optical wavelengths than the rest of their hosting galaxies. Moreover, their spectra typically showed a non-thermal highly-polarized emission with a bump in the *UV* band which could not be ascribed to stars. Other unmistakable footprints of Seyfert galaxies were the presence of prohibited emission lines with *Full Widths at Half Maxima FWHM*  $\sim 200 \div 500 \text{ km s}^{-1}$  and permitted emission lines with *FWHM* up to  $\sim 10^4 \text{ km s}^{-1}$ . This dichotomy in line widths originated a first classification of Seyfert galaxies: *type 1* sources were the ones with broad emission lines of *FWHM*  $> 10^3 \text{ km s}^{-1}$ , occurring in a  $\sim 20\%$  of the cases, while *type 2* galaxies had *FWHM*  $< 10^3 \text{ km s}^{-1}$ .

The nuclear regions of Seyfert galaxies which turned out to be part of the more general class of *Active Galactic Nuclei* (AGN), were not only discovered to be just quite strange and powerful lightbulbs: also absorption lines had widths far greater than the escape velocity from the bulge, probing the presence of winds of highly relativistic particles injected in the surroundings.

Similar properties were later observed in the radio band of some elliptical galaxies: the so-called radio galaxies showed a luminosity in the radio waveband largely exceeding the typical values of  $\sim 10^{39} \text{ erg s}^{-1}$  (see e.g. Becker et al. 1995 for a review of radio AGN properties in the FIRST database), up to 5 orders of magnitude, and were often associated with powerful and even extremely collimated relativistic jets of particles forming enormous radio lobes up to some *Mpc* away from their central point-like origin.

It is certainly the discovery of such strange objects that gave birth to the hypothesis that the central engine, especially during particular active phases of a galaxy's life, could play an important or maybe a leading role in igniting star formation bursts by perturbing molecular clouds through radiation pressure or relativistic winds, thus also affecting metallicity, dust

---

density and the subsequent global emission properties of the whole galaxy.

Another milestone for the comprehension of the nature of the central compact objects in AGN was the detection of quasars. The first one was discovered as the optical counterpart of the radio source 3C273 (Schmidt 1963). Its cosmological redshift of  $z = 0.158$  made it one of most distant and luminous objects observed until then and, as I will widely discuss in this thesis, large observational campaigns during the last fifty years permitted to discover hundreds of thousands of quasars in the deep sky with redshifts up to  $z = 7.085$  (Mortlock et al. 2011). The rapidly variable AGN lightcurves testified the tiny size of the emission region compared to that of the host galaxy, from a few light hours to a few light years, according the the luminosity of the AGN.

The same surveys also permitted a statistically significant demography of active galaxies, which represent to this day a  $\sim 15\%$  of all the known galaxies. In Section 1.3 we will briefly recall how apparently different observational properties can indeed be explained by a relatively simple unified model for all active nuclei. As for now, it is sufficient to remind that there is a clear trend of the AGN number density as a function of cosmological redshift: a redshift of about 2 appears to mark the “golden ages” of galaxies’ nuclear activity, indicating that a large percentage of galaxies (if not all) lived at least a period of AGN emission and suggesting that the smoking guns can still be hiding themselves at the center of galaxies in the local universe.

## 1.1 Supermassive black holes in nearby galaxies: observational evidences and detection methods

It is by now well accepted that the only physical process that can explain the observed AGN phenomenology is gas accretion onto supermassive black holes (SMBHs). The first suggestions about this fueling mechanism are framed around the 60's (Hoyle & Fowler 1963; Salpeter 1964; Zel'dovich 1964; Lynden-Bell 1969; Lynden-Bell & Rees 1971). In this section a very brief summary of the reasons for this assumption will be provided.

First of all, SMBHs are black holes with mass  $M_{BH} > 10^6$ . Therefore we distinguish them from stellar BHs (with masses of the order of  $\gtrsim 10 M_{\odot}$  originated by stellar seed of mass greater than  $20 \div 30 M_{\odot}$ ) and intermediate mass black holes (IMBH), with masses of  $\sim 10^3 \div 10^4 M_{\odot}$ , maybe originated by collapsing zero-metallicity Population III stars and/or by mergers (van der Marel 2004). We thus expect to find them in regions of maximal stellar and gas density, such as galactic nuclei. SMBHs are now believed to reside in the majority (if not the entirety) of the centers of galaxies.

A SMBH detection necessarily requires to observe the consequences of its presence on the surrounding material. Gas, dust and stars within the sphere of influence, defined by

$$r_{is} = \frac{GM_{BH}}{\sigma_{\star}^2} = 0.42'' \left( \frac{M_{BH}}{10^8 M_{\odot}} \right) \left( \frac{\sigma_{\star}}{200 \text{ km s}^{-1}} \right)^{-2} \left( \frac{D}{5 \text{ Mpc}} \right)^{-1}, \quad (1.1)$$

(see Binney & Tremaine 1987) where  $\sigma_{\star}$  is the velocity dispersion of the stars in the nuclear region and  $D$  the distance of the galaxy, can probe the presence of an attracting source through photometric and spectrometric indicators. Both stellar and gas kinematics have their pros and cons. Stars are ubiquitous and less sensible to the turbulence of the surrounding material so that we can fairly assume that their orbits are mostly governed by the gravitational potential of the BH. On the other hand, they have a low surface brightness, thus needing large exposure times to be traced, and their motions require a careful dynamical analysis to be interpreted. Gas, on the contrary, has higher surface brightness and easier dynamical models. Moreover gas clouds can provide informations about a region that is even closer to

the black hole and its emission lines are almost ubiquitous in the first hundreds of parsecs around the center of spiral and S0 elliptical galaxies (see e.g. Ho et al. 2003 and references therein). Gas is unfortunately very sensible to winds, radiation pressure, magnetic fields and turbulence.

However, discerning between what is actually originating the gravitational potential well can be tricky. The detection of a black hole can only be provided by both a spatial constrain and a mass measure: the additional dark mass required to explain the observed stellar orbits has to be confined within a region small enough to exclude stable clusters of smaller massive dark objects. Therefore, it should be clear that SMBHs detection and mass measurements are feasible through kinematical methods only for nearby galaxies. Nevertheless, it should be noted that the high mass tail of the BH mass distribution is far easier to be measured as it is characterized by larger spheres of influence. Thus, even in local universe where we expect to collect a statistically significant sample of SMBHs to infer constraints for galaxy evolution models, we have to face an inevitable bias.

A key parameter appears then to be the ratio  $\frac{r_{is}}{\sigma_{psf}}$  between the radius of the sphere of influence and the effective Gaussian dispersion radius of the point spread function of the observations (Kormendy & Kennicutt 2004). Both high spatial and spectral resolutions are required to get accurate density distribution of the stars and velocity dispersions. Only with the arrival of CCD on spectrographs ratios  $\frac{r_{is}}{\sigma_{psf}}$  of the order of unity or greater could be reached. Since then, after almost thirty years of technical improvements and observations, kinematical methods in SMBHs detections and mass measurements could only be applied for  $\sim 50$  local galaxies (see for example Sani et al. 2011) and the inferred mass distribution is suspiciously not symmetric, suggesting a possible bias in the sample.

Obviously, the very best results are reached with our own galaxy. In this case, individual stars orbiting very close to the galaxy center can provide an accurate measurement of BH mass. With the recent HST and ground-based adaptive optics (AO) era, effective resolutions up to  $\sim 0.01''$  became feasible. For instance, in our own Galaxy it was possible to map a full orbit of the star S2 around the BH, with a pericenter radius of about 122 AU  $\simeq 1400 r_S$  (where  $r_S$  is the Schwarzschild radius of the BH). Also star S16 is a very promising object

that has been followed but has not yet completed a complete orbit since its first detection. For the SMBH in our Milky Way, we then have (Genzel et al. 2010):

$$M_{BH} = 4.30 \pm 0.20(stat.) \pm 0.30(syst.) \times 10^6 M_{\odot} \quad (1.2)$$

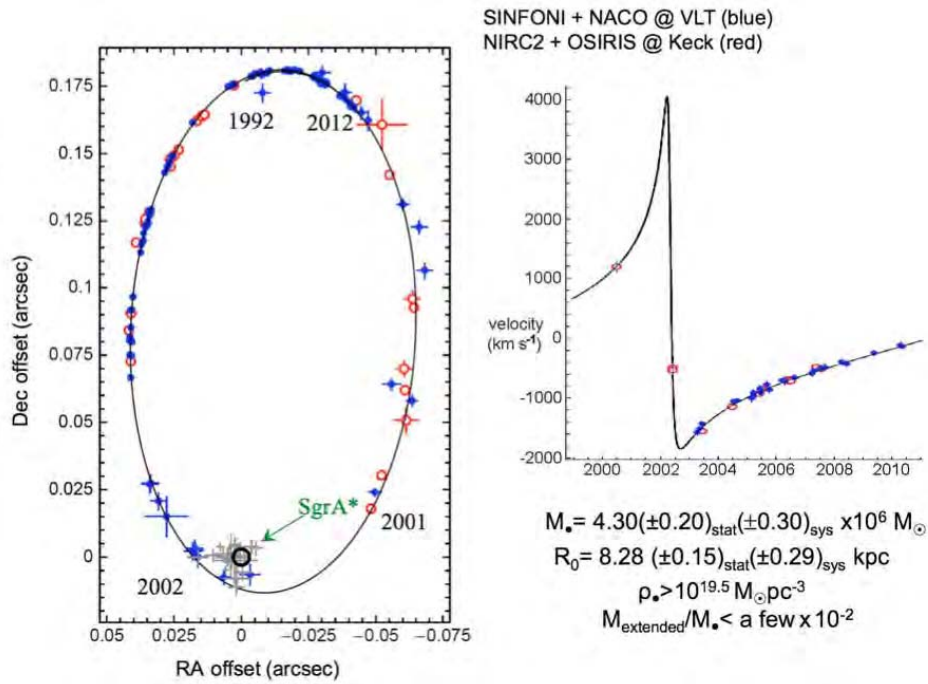


Figure 1.1 Orbit of star S2 around Sgr A\* (*left panel*) and radial velocity (*right panel*). Observations from 1992 to 2012. The grey crosses correspond to the positions of the observed Sgr A\* IR-flares, while *blue* and *red* points denote the data from NTT/VLT and Keck, respectively. Updated data from Genzel et al. 2010.

Another strong SMBH detection is certainly the one in NGC4258 through radio interferometry of water maser emission from the accreting gas (Miyoshi et al. 1995). In this case exceptional angular resolution permits a very good estimation of mass in spite of the small size of the BH. Recent mass measurements through water masers provided some other excellent results (Kuo et al. 2011).

Anyway, the *small number* of available and affordable measurements is a critical issue in deriving significant informations about the correlations between SMBH mass and global

properties of the host galaxies. With HST high resolution, BHs were found in many galaxies and adaptive optics (AO) in the IR band, later, also permitted better results in late type galaxies, overcoming difficulties connected to high dust column densities. BH demographics became finally handy. In addition, some improvements in kinematical techniques are luckily helping to get larger SMBHs mass samples in local galaxies.

About stellar dynamics, one of the main difficulties is represented by the unknown anisotropy in velocity distribution. Kormendy & Richstone (1995) explain how BH mass measurements derived by the collisionless Boltzmann equation depend on the radial and azimuthal components of the velocity dispersion. Anisotropy appears to have heavy consequences in BH mass estimates especially in core elliptical galaxies. To take into account anisotropy, we can model galaxy core dynamics by using the so-called Schwarzschild's orbit superposition method. Stellar kinematics are derived by the numerical computations of randomly distributed orbits which are then combined to fit the observed light and velocity distributions; such a dynamical model depends on several free parameters, such as the stellar mass to light ratio, energy, angular momentum and obviously the mass of the central BH. Recently, also the dark matter halo contribution has been included in computations in order not to underestimate BH masses, especially in ellipticals with cores.

Regarding gas dynamics, as mentioned above, the influence of turbulence, magnetic field, radiation pressure and outflows makes it necessary a cross check of the derived BH masses with the estimates coming from stellar kinematics, when available. A recent comparison by Kormendy & Ho 2013a can show a potential systematic underestimation of BH masses and larger uncertainties, thus gas dynamics could apparently be considered less reliable when compared to stellar dynamics (see Figure 1.2). However, the complexity of stellar dynamical models require a cross-check that can only be provided by gas kinematical measurements.

Another powerful tool that can provide detailed informations about the innermost region of the AGN is certainly given by the X-ray spectrum. Fe  $K\alpha$  fluorescent line (with rest-frame energy between 6.4keV and 6.96keV) is its most prominent feature and is thought to be originated by the accretion disk of an internal SMBH (see Section 1.4 for details on the internal structure of an AGN). Fe  $K\alpha$  line profiles have been investigated by many authors

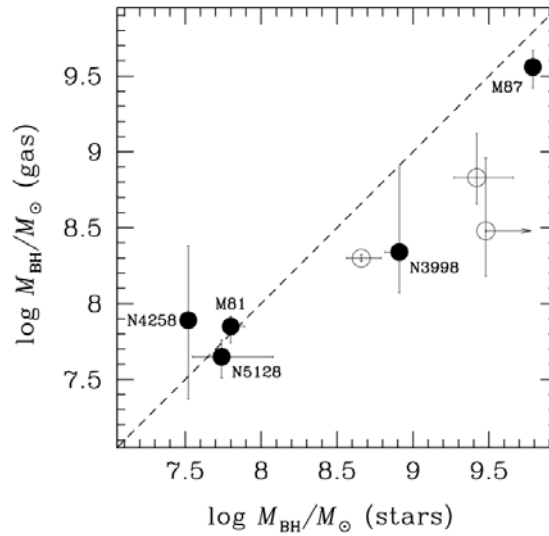


Figure 1.2 Comparison between BH mass measurements from stellar and gas dynamics. Open circles represent the objects with less reliable estimates.

to constrain the BH mass and spin, the size, the inclination and the ionization state of the accretion disk (see, e.g., Tanaka et al. 1995; Nandra et al. 1996, 1997, 1999; Fabian et al. 2000; Nandra et al. 2007; Fabian et al. 2009). In particular, each ring in the accretion disk is thought to produce a double-horned profile due to the contributions by the approaching and receding sides of the disk with respect to the observer. The gravitational potential in the emitting region is indeed strong enough to cause a relativistic beaming of the emission, enhancing the blue component with respect to the red one. The overall effect is given by an asymmetric broad double-peaked profile (Fabian et al. 2000). An example of this distortion is observed in MCG-6-30-15 (Tanaka et al. 1995; Wilms et al. 2001; Fabian et al. 2002; Vaughan et al. 2004).

The estimates of the accretion disk sizes and the very short timescales observed in the lightcurves of many active nuclei (see Section 1.6.1 for discussion) can strongly support the presence of an inner SMBH and can in principle let us investigate the internal structure of the AGN even when the BH sphere of influence is not resolved.

For what concerns the available measurements in local galaxies, only in the two cases of Milky Way and NGC4258 we can certainly conclude the presence of a SMBH, due to the

exceptional spatial resolution achieved. In all the other cases, it can be difficult to definitively rule out the hypotheses of other dark objects, especially exotic ones such as boson balls (see for example Liebling & Palenzuela 2012). By assuming that every galactic nucleus is hosting a SMBH as a relic of previous AGN activity we make a very strict (but reasonable) assumption that is indeed at the basis of every demographic study of SMBHs and has strong influence on the inferred BH-galaxy (co)evolution model.

## 1.2 SMBH-galaxy correlations

Several correlations have been observed between SMBH masses in local universe and some global properties of the host galaxies, starting from the first suggestion by Kormendy & Richstone (1995) about the scaling relation between  $M_{BH}$  and the absolute magnitude of the bulge (or of the entire galaxy in case of an elliptical) in the B band,  $M_{B,bulge}$ . Although, in that work, BH masses were just a few and with high uncertainties, a clear evidence that SMBHs' accretion could condition and be conditioned by the host galaxies far beyond the sphere of influence was a breakthrough in galaxy evolutionary studies.

After that starting point, three years later Magorrian et al. (1998) discovered a link between the masses of the black holes and those of the bulges. That correlation was later corrected, for Magorrian BH masses being systematically overestimated. With two independent papers, Ferrarese & Merritt (2000) and Gebhardt et al. (2000a) claimed another fundamental scaling relation, the one between black hole masses and the stellar velocity dispersion in the bulge,  $\sigma_*$ , while Marconi & Hunt (2003) discovered a relation between  $M_{BH}$  and bulge luminosity in the NIR K band,  $L_{K,bulge}$ .

$M_{BH} - \sigma_*$  seemed at first to be the best correlation (i.e. the one with minimum intrinsic scatter, of the order of  $\sim 0.3$  dex). Marconi & Hunt (2003) showed indeed how BH-galaxy scaling relation all have an intrinsic scatter of the same order and that differences are mainly due to the high uncertainties on BH mass measurements. Moreover, it was shown that these correlations are all linked to galaxies scaling relation and can be derived the one from the others when considering the Fundamental plane and the Faber-Jackson relation.

All the correlations above share the common flaw of the sample being quite scarce (just 64 galaxies with a reliable estimate of  $M_{BH}$ , Figure 1.3 provided by Graham et al. 2011, and Figure 1.4, by Gültekin et al. 2009), with high uncertainties in many cases and clear biases. For example, there are a very few detections of small mass BHs and most of the

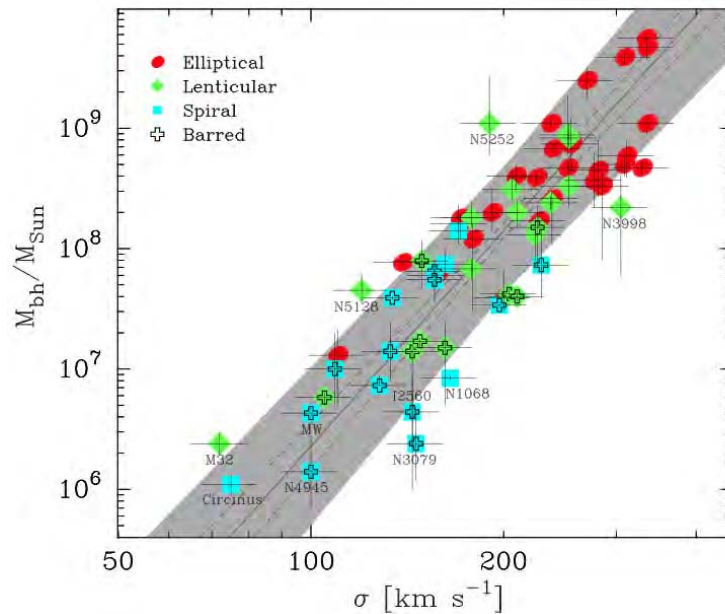


Figure 1.3 Updated  $M - \sigma$  correlation for the 64 sources with "direct" mass estimates (derived from stellar or gas dynamics or masers), from Graham et al. (2011). The solid line is obtained from a regression of  $\log M_{BH}$  on  $\log \sigma$ , assuming a 10% uncertainty on  $\sigma$ . The dashed corresponds to the  $1\sigma$  uncertainty on the correlation, and the grey area shows the rms scatter of the correlation.

observations regard early-type galaxies, with a few spirals. Moreover, it is not clear whether small BHs can lay in massive galaxies, thus if the observed  $M_{BH}$ -galaxy relations can be just upper envelopes. Moreover, recent papers reveal that pseudo-bulges do not follow the same correlations of ordinary galaxy bulges (e. g. Kormendy & Kennicutt 2004; Kormendy & Ho 2013a) and that there could be a cosmological evolution of BHs-galaxies relations, strongly affected by biases towards selecting the most massive SMBHs and/or the most luminous and gas-rich galaxies (see Figure 1.5, by Lamastra et al. 2010).

Indeed, the sample of very accurate BH masses is so poor that it would be impossible to derive a direct estimation of statistical properties of local BHs, such as the [Super Massive]

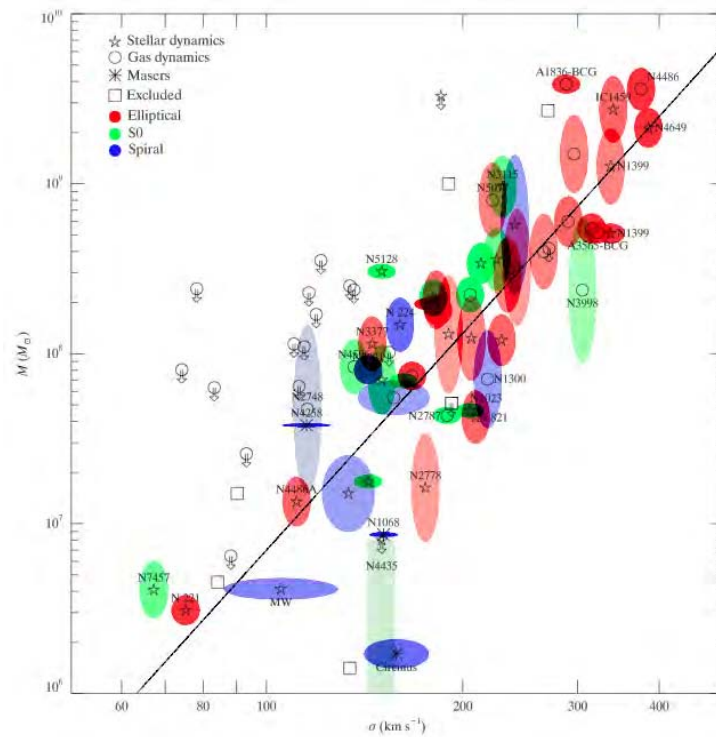


Figure 1.4 The  $M-\sigma$  relation for galaxies with direct mass estimates (derived from stellar or gas dynamics or masers), from Gültekin et al. (2009). The *black solid line* is the best fit relation to the data sample.

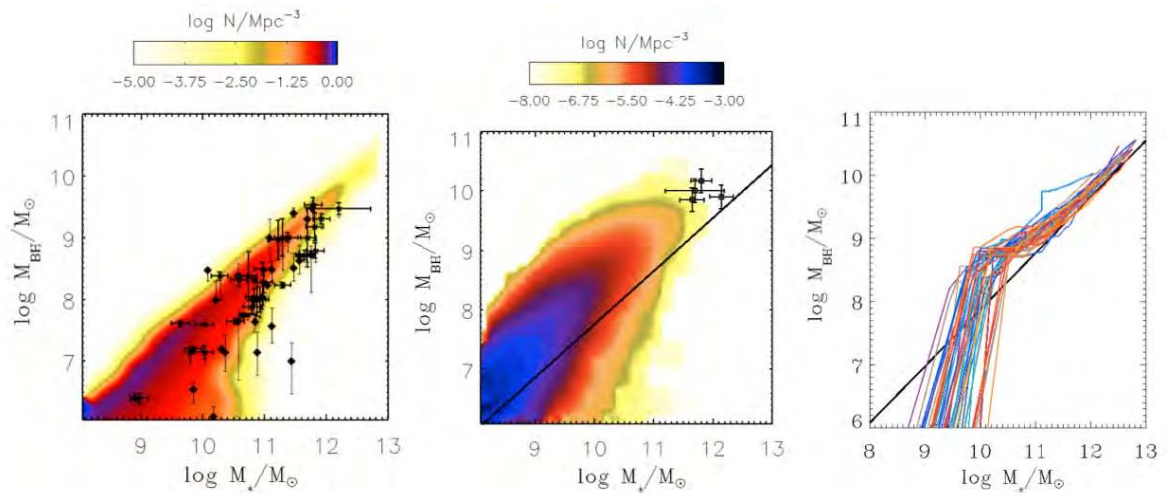


Figure 1.5 *Left* panel: The local predicted  $M_{BH}-M_*$  relation, with a color code representing the BH number density (per  $\text{Mpc}^3$ ) in each  $M_{BH}-M_*$  bin. Data points are from Marconi & Hunt (2003) and Häring & Rix (2004), where  $M_*$  is derived from the virial relation of Cappellari et al. (2006). *Central* panel: the prediction of the same relation at  $z=4$ . Data points are broad-line AGN with their host galaxies in the range  $4 \leq z \leq 6$ . The *black* solid line represents the best estimate for the local correlation. *Right* panel: some evolutionary paths in the  $M_{BH}-M_*$  plane followed by BHs and their host galaxies up to  $z=0$  and  $M_{BH} = 10^{10} M_{\odot}$ . Picture from Lamastra et al. (2010).

*Black Hole Mass Function* (BHMF), or its integrated BH mass density without using the BH-galaxy correlations described above. Yu & Tremaine (2002) and Marconi et al. (2004) already showed how easily observable distributions, for example the galaxies' luminosity distributions from Nakamura et al. (2003) or Devereux et al. (2009), conveniently converted into *bulges* luminosity distributions, can be convolved with the local correlation between BH masses and bulge luminosity (e. g. Graham et al. 2007 or Gültekin et al. 2009) to obtain the local BHMF and its integrated mass density.

### 1.3 AGN taxonomy

In Section 1.1 we anticipated that AGN are believed to be fueled by gravitational accretion onto supermassive black holes. Many arguments, both theoretical and observational, support this assumption. This Section intends to summarize some of them, recalling the main evidences for the well known *Unified Model*, highlighting its strong points and some critical issues still unsolved.

The requirement for SMBH accretion is not only due to arguments about the instability of almost any other massive compact object constrained in a region of some hundreds of AU: also the observed bolometric luminosities can only be explained with radiative efficiencies as those that can be obtained from accretion onto Schwarzschild or fast rotating Kerr black holes. Moreover, assuming for simplicity an isotropic distribution of radially accreting material, mostly composed by hydrogen atoms only subject to gravitation and radiation pressure (the former mainly acting on the protons and the latter mainly acting on the electrons) and considering an isotropically radiating point source, the equilibrium between gravitational force and radiation pressure defines the upper limit of the Eddington luminosity, which gives in turn a lower limit for the mass of the central source:

$$M_{BH} \gtrsim 10^6 M_{\odot} \left( \frac{L_{bol}}{10^{44} \text{ erg s}^{-1}} \right) \quad (1.3)$$

a few tens of Schwarzschild radii for such masses are of the same order of magnitude as the sizes of the emitting sources, derived by the variability of the light curves.

In this context, although there is not a universally accepted threshold, the Eddington ratio, i.e. the ratio of the bolometric luminosity of an AGN to the Eddington luminosity can be considered a good parameter to discern active from quiescent galaxies.

It is the detail of the accretion process that can explain the remarkable variety of active nuclei subclasses, each identified by specific observed emission features. In the following, it will be presented a possible although not univocal classification.

As a first distinction, we separate the sources depending on the amount of the emission in the radio band. This distinction has both a physical and an historical reason, since it was the identification of Radio Galaxies which first triggered the study of AGN as a particular class of objects fueled by a relativistic engine. We consider as Radio-loud sources the nuclei whose emission is characterized by a ratio of radio (5 GHz) to optical (B-band) flux of the order of 10 or greater. Radio-quiet nuclei lay below this limit (Kellermann et al. 1989).

### 1.3.1 Radio-quiet Nuclei

Radio quiet sources represent the vast majority of the observed AGN, with a percentage of  $\sim 80 \div 85\%$ . This values appear to be indeed dependent on the optical- and X-band emission: for example, for high optical luminosities ( $M_B \lesssim -24.5$ ) radio quiet sources drop to  $\sim 50\%$  of the whole population (e.g. Padovani 1993; La Franca et al. 1994; Goldschmidt et al. 1999; La Franca et al. 2010; Elvis et al. 2012; Bonchi et al. 2013).

#### Seyfert Galaxies

This class obviously include the galaxies first discovered by Carl Seyfert in the 40's. The photometric fingerprint for these objects is the presence of a very bright star-like nucleus surrounded by a well resolved host galaxy. As previously mentioned, we separate them in two (or more, see e.g. Osterbrock 1981) subclasses: Seyfert 1 (Sy1) galaxies, which show

broad permitted and narrow forbidden emission lines, and Seyfert 2 (Sy2) galaxies, which do not show broad lines, at least in unpolarized light. The partition between the two subclasses is arbitrary set to a value of  $FWHM > 1000 \text{ km s}^{-1}$  for a permitted line to be considered *broad*.

While forbidden lines are only observed with narrow profiles (generally with  $FWHM$  of the order of  $\sim 10^2 \text{ km s}^{-1}$ ), permitted lines typically show both a narrow and a broad component, with  $FWHM$  often exceeding  $10^4 \text{ km s}^{-1}$ . Moreover, since the forbidden transitions have a low probability of occurrence, they can only be observed in low density gas clouds, with a low rate of collisional de-excitation. Broad lines have to be emitted by high density fast moving gas clouds, where broad forbidden lines are collisionally suppressed.

### **Narrow Line Seyfert 1 Galaxies**

In this class we identify a particular subset of Seyfert 1 galaxies which have, unusually, an  $H\beta$  emission line with  $FWHM < 2000 \text{ km s}^{-1}$ , thus giving a narrow line, but still have an  $[OIII]5007/H\beta$  flux ratio of less than 3 (and this is typical of Seyfert 1 galaxies). They also have strong FeII emission lines in optical band and a steeper X-ray spectrum if compared with common Sy1 nuclei.

### **Radio-quiet Quasars**

Although luminous quasars were identified as highly redshifted point-like optical counterparts of powerful radio sources,  $\sim 90\%$  of these sources have radio to optical ratios low enough to be included in the Radio-quiet class. Kellermann et al. (1989) suggested to use, in particular, the ratio  $R_{r-o}$  of the observed fluxes at 5 GHz and  $4400\text{\AA}$ , defining as Radio-quiet sources those with  $R_{r-o} \lesssim 10$ . Spectral features are a continuum extended up to the X or even the Gamma band, with IR, UV and X bumps and very broad emission lines. All of them have short timescales in their light curve fluctuations.

### BAL Quasars

A significant fraction of radio-quiet AGN have broad absorption features in their optical and ultraviolet spectra, and so are known as BAL (Broad Absorption Line) quasars (Turnshek 1984). A parameter that is commonly adopted to identify BAL-QSOs is the *balnicity index* (BI), introduced by Weymann et al. (1991), which for BAL sources differs from 0. The estimate of the fraction of BAL-QSOs, based on several absorption lines (such as  $\text{CIV}\lambda 1550$ ,  $\text{SiIV}\lambda 1400$ ,  $\text{AlIII}\lambda 1860$  and  $\text{MgII}\lambda 2800$ ) has been performed by several authors (e.g. Hewett & Foltz 2003; Reichard et al. 2003; Scaringi et al. 2009; Knigge et al. 2008; Gibson et al. 2009; Allen et al. 2011) and varies from  $\sim 10\%$  to  $\sim 40\%$ . These estimates appear to be strongly dependent on the S/N ratio of the adopted sample, on the line profile fitting technique and on redshift.

The interpretation of such sources in the unified model is not unique (see, e.g., Elvis 2000).

### ULIRGs

In the *Ultra Luminous Infrared Galaxies* the spectrum is dominated by the infrared emission, originated by cool dust reprocessing of incident light. It is nowadays accepted that most of them are likely be powered by starbursts but some of them could also host an obscured AGN. Indeed, the fraction of AGN appears to increase at increasing far-infrared luminosity (see e.g. Genzel & Cesarsky 2000). We therefore include them in AGN classification as they could represent a piece of the unification puzzle.

### LINERs

LINERs are Low Ionization Nuclear Emission-line Regions. Spectroscopic features are similar to the the ones typical for Seyfert 2 galaxies, with some exceptions: LINERs show some prominent but narrow low ionization lines, such as  $[\text{OI}]\lambda 6300\text{\AA}$  and  $[\text{NII}]\lambda 6548\text{\AA}$ . It should be noted that LINERs are not necessarily AGN as in many cases their emission can also be explained with starburst-driven winds or shock-heated gas (Heckman et al. 1987; Filippenko & Terlevich 1992), which may also explain the relatively large width of some emission lines

which are sometimes found in their optical spectra.

### 1.3.2 Radio-loud Nuclei

After their first detections, radio-loud galaxies are still generally detected with optical counterparts given by giant ellipticals. Not rarely, the high-dynamic-range CCD images of the host galaxies reveal morphologies that are rather complex and disturbed. The persistent collimated jets and lobes we already discussed in the Introduction are associated with relativistic motion of electrons in high magnetic fields. There are several attempts to divide them into subclasses, depending on the spectral or photometric feature we look at. We just mention one of them: by defining the ratio  $r_{FR}$  between the lobes separation and the size of the central source at 178 MHz we have the distinction between the so-called Fanaroff-Riley Type I and Type II Galaxies.

#### Fanaroff-Riley Type I Galaxies

These galaxies have ratios  $r_{FR} < 0.5$ . In these sources, lobes are generally fainter than the internal jet region. Two-sided jets are detected in the vast majority of the cases. Hotspots in the jets eventually show “superluminal” motion, thus strongly indicating a small viewing angle with respect to the line of sight.

#### Fanaroff-Riley Type II Galaxies

In these cases  $r_{FR} \geq 0.5$ . The overall luminosity is far higher than in FR I galaxies, but the jets to lobes luminosity ratio is below the typical values of FR I sources. Jets are less frequently detected (but ubiquitous in Radio-loud Quasars) and, when observed, are typically less bent with increasing distance from the central source.

Spectroscopic features of the central sources permit then to distinguish between *Broad Line Radio Galaxies* and *Narrow Line Radio Galaxies*, which can be considered as Radio-loud counterparts to the Seyfert 1 and Seyfert 2 galaxies respectively.

It has been found that nearly all sources with  $L(178 \text{ MHz}) \lesssim 2 \times 10^{25} h_{100}^{-2} \text{ W Hz}^{-1} \text{ str}^{-1}$  belong to class I, while brighter sources usually belong to class II. The separation is not sharp and there is some overlapping in the two classification criteria (structure and luminosity).

### Blazars

A separate class has to be reserved to a small fraction of galaxies showing an extremely short variability timescale ( $\sim$  a few days) and high levels of continuum polarization. We collectively call these objects Blazars, and within them we find several subsets: the **BL Lacertae (BL Lac)** galaxies are Radio-loud very luminous AGN, with no strong emission or absorption features; the **Optically Violently Variable (OVV)** quasars are very similar to BL Lac but show broad emission lines. All of them show high brightness temperatures and apparently superluminal velocities of compact radio hotspots, e.g., see Urry & Padovani (1995) and references therein.

## 1.4 Evidences for a Unified Model of AGN structure

In the previous Sections we briefly described the classification criteria for nuclear activity and the several classes arising from an observational classification. From the first detection of Seyfert Galaxies, it took more than thirty years to put forward a plausible physical description of the central engines responsible for sustaining nuclear activity. It became necessary to discover several classes of luminous and, for some reason, weird nuclei to glimpse, beyond the multitude of differences, a common denominator. The reason for this delay has to be found in the biases introduced by each observational technique: the first radio telescopes only selected very luminous radio-loud galaxies, for example, which could hardly be correlated to the observed Seyfert Radio-quiet galaxies.

It was only later, with the beginning of broad-band photometry, and the resolution improvements of the spectrographs that it was possible to discover several new observational features, preparing the ground for a unification theory.

The first suggestion was proposed by Rowan-Robinson (1977): by comparing the observed

spectra of active galaxies and their luminosity functions, the author suggested a unification between all the active sources known at that time: radio galaxies, Seyfers and quasars. The paper explained in particular the distinction between Seyfert 1 and Seyfert 2 galaxies with a more significant dust reprocessing in the latter resulting from an orientation effect of axisymmetric sources. A proof for this assumption was provided a few years later by Antonucci & Miller (1985) who discovered broad lines in the polarized spectra of Seyfert 2 galaxies, thus demonstrating that the Seyfert 1 and 2 classes are substantially the same kind of objects, except for the fact that Seyfert 2 broad emission lines originating from high velocity gas clouds are suppressed by dust obscuration along the line of sight and are only visible through reflection. The most plausible framework appeared to be given by a randomly oriented toroidal dusty structure.

A clear picture appeared then in Urry & Padovani (1995). A unique fundamental axisymmetric structure, made up of several components (see Figure 1.6), each responsible for one or more emission features, could finally explain many details of the vast phenomenology in terms of inclination with respect to the line of sight.

At the center we find a **SMBH**, with masses between  $10^6$  and  $10^{10} M_{\odot}$ , whose gravitational potential dominates the kinematics within the sphere of influence.

In the immediate surroundings the gas gathers in a thin (but optically thick) hot Shakura-Sunyaev **accretion disk**, from which it gradually feeds the SMBH by losing angular momentum because of magneto-rotational instabilities. According to the virial theorem, roughly half of the gravitational potential energy of the accreting mass is converted in kinetic energy, the other half powering detectable radiative emission. The ratio of the emitted bolometric luminosity to the mass accretion rate (in units of  $c^2$ ) is the radiative efficiency and depends on the BH spin, ranging from  $\sim 0.056$  in the case of a Schwarzschild BH to  $\sim 0.42$  in the case of a maximally rotating Kerr BH. The accretion disk emits mostly in optical and UV bands, while its surrounding hot corona is responsible for the hard X-rays emission. The location and structure of the X-ray corona is still unknown.

The continuum luminosity is thought to be emitted almost isotropically, therefore the external components are in this picture fully responsible for the observative differentiation between

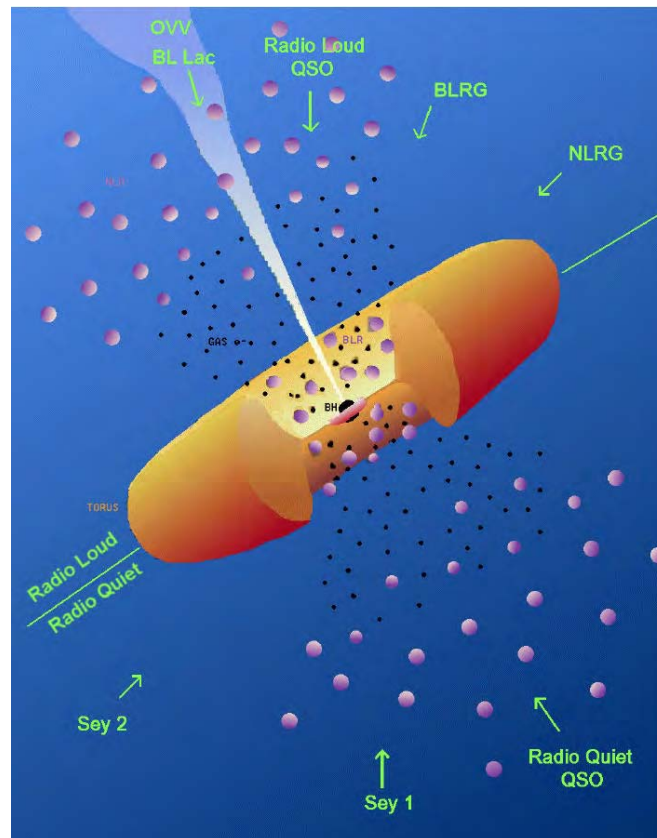


Figure 1.6 The Unified Model proposed by Urry & Padovani (1995). The observed differentiation in AGN classes is interpreted as a consequence of radio luminosity and orientation of a same fundamental structure with respect to the line of sight. The central SMBH is surrounded by an accretion disk (in *pink*) and, at larger distances, by a toroidal dusty obscuring region (in *orange*). The gas clouds fast orbiting close to the BH populate the BLR, while farther clouds populate the NLR.

AGN classes. In particular, gas and dust are thought to populate a very high number of clouds orbiting around the BH. This circumnuclear absorbing medium has been shown to be clumpy through several observations of X-ray absorption variability (see e.g. Risaliti et al. 2002; Risaliti et al. 2007; Risaliti et al. 2011) and through IR observational properties arguments (see Nenkova et al. 2002; Elitzur & Shlosman 2006; Nenkova et al. 2008). The clouds which are closer to the BH have obviously the higher average temperature and velocity and populate the so called **Broad Line Region (BLR)**. Here the gas density is large enough ( $n_e \gtrsim 10^9 \text{ cm}^{-3}$ ) to let the gas emit Doppler broadened permitted lines. X-ray absorption variability observations during eclipsing events have also shown that each BLR cloud should have a cometary-shape geometry. We will extensively discuss this region, its composition, extension and geometrical structure. In Section 1.6 we will explain how the BLR can provide very useful indirect measurements of the BH mass and in Chapter 2 we will then examine in detail our simulations of BLR structure and composition in order to test observative results about the BLR size and the effects that dust has on the overall observed emission.

More distant clouds ( $\sim 1 \text{ pc}$ ) close to the equatorial plane have lower densities and form an optically thick region, the **dusty torus**, which efficiently intercepts most of the radiation emitted by the accretion disk and contributes to the overall AGN emission with reprocessed IR light. Many authors have investigated the location and the internal structure of this region (e.g. Jaffe et al. 2004; Suganuma et al. 2006; Tristram et al. 2007; Nenkova et al. 2008; Raban et al. 2009; Mor et al. 2009; Burtscher et al. 2013 and many others) and recent studies have called into question the naive assumption of the obscuring region being necessarily toroidal (Elitzur & Shlosman 2006) and aligned with the accretion disk (see Raban et al. 2009; Risaliti et al. 2011).

The dusty region is thought to intercept the isotropic emission of the accretion disk along the torus equatorial plane. The ionizing photons are therefore allowed to reach only the clouds within an **ionization cone** around the AGN symmetry axis, up to distances of  $\sim 10 \div 100 \text{ pc}$ . The latter have lower densities and lower velocities if compared to BLR clouds, therefore they do not contribute to the observed broad lines. This region is thought instead to originate the narrow emission lines by forbidden transitions, and is therefore called **Narrow Line**

**Region (NLR).**

A significant fraction ( $\sim 15\%$ ) of the active nuclei, as already mentioned, also produces extremely collimated **jets** of highly relativistic particles that can reach enormous distances (up to  $\sim 1 Mpc$ ). Jets are present in all the Radio-loud AGN and eventually show radio hot-spots in apparently superluminal motion.

Moreover, this basic structure is able to explain most of the observed features of different AGN classes as an orientation effect of the AGN symmetry axis with respect to the line of sight. In particular, what is assumed to be strongly dependent on the observer's position is the amount of radiation, coming both from the accretion disk and from the recombination and deexcitation of photoionized atoms in BLR clouds, which is intercepted and absorbed by the dusty torus or by optically-thick dense gas clouds close to the equatorial plane.

Therefore, Seyfert 1 and Seyfert 2 galaxies are substantially the same kind of sources, but Seyfert 1 are seen "face on" (thus with small viewing angles), while Seyfert 2 are seen "edge on". In general, "face on" sources are also referred to as Type 1 AGN, while "edge on" are called Type 2 AGN. Obviously, the range of inclination angle between the extremal conditions of "face on" and "edge on" allows every intermediate situation to occur. These scenarios correspond to a gradual transition from high to low ratios of broad to narrow emission lines strengths. Osterbrock (1981) describes these intermediate conditions by refining the Seyfert classification: 1.2, 1.5, 1.8 and 1.9 Seyfert types correspond to a broad component of the  $H\beta$  line which gradually becomes weaker with respect to the corresponding narrow component. The broad emission lines from the inner clouds of the BLR are strongly suppressed in the latter cases and can only be recognized in polarized light after being scattered by electrons and dust grains. A still open issue about torus absorption concerns the larger suppression of emission lines with respect to the incident continuum radiation. Moreover, in nearly "edge on" sources the observed continuum emission appears to have an unpolarized featureless component (60%–90% of the overall continuum luminosity) which is thought to be originated by free-free emission in the scattering region itself. The photons from the accretion disk illuminating the atoms in the torus are absorbed and re-emitted towards the observer.

The emission from the narrow line region is on the other hand not suppressed by the torus,

for its being produced by clouds which are considerably far from the torus plane and is therefore observable both in Type 1 and in Type 2 AGN.

A key test for the Unified Model is the consistency between the predicted and the observed space density ratio of any orientation selected subclass to the whole population. Space densities are nevertheless often hard to be measured as they are strongly dependent on possible observational biases and also depend on several structural parameters of the AGN: for example, a non-trivial distribution of AGN opening angle of the dusty torus or a non-perfectly isotropic angular distribution of the continuum luminosity can originate mistakes in AGN classification, thus distorting the space densities estimates.

An even more unsolved issue is the explanation of the asymmetry between Radio-loud and Radio-quiet populations: the ratio between their number densities (1 : 10) is not easily explained by orientation. Theories that try to reproduce this dichotomy are referred to as Grand-unification models. In the subset of Radio-loud sources, however, the differences between core- and lobe-dominated AGN can again be represented as an orientation effect: core-dominated nuclei often show radio hot-spots in superluminal motion and usually have one-sided jets, which are all features due to relativistic effects of Doppler boosting and dimming in case of small viewing angle.

## 1.5 SMBHs growth and AGN feedback

BHs-galaxies correlations represent an incontrovertible evidence of mutual mass and energy exchanges during violent phases of SMBHs' accretion and feedback onto the host galaxies (see e.g. Soltan 1982; Yu & Tremaine 2002; Marconi et al. 2004; Merloni & Heinz 2008; Hopkins et al. 2009; Lamastra et al. 2010; Shankar et al. 2013). In this framework, AGN are therefore temporary violent interludes in the quiescent state of an ordinary galaxy core. Local SMBHs have therefore to be the result of such previous active phases.

An elegant demonstration of this assumption is given by the so-called Soltan argument (Soltan 1982): by assuming that BH accretion mostly takes place during AGN phases, the

AGN BHMF can be constrained to the AGN luminosity function. The latter can be derived from the X-ray background, which is mostly due to AGN emissions and can therefore be considered as a good tracer of AGN phases at all redshifts. The inferred BHMF can be integrated over cosmic time to obtain a prediction for the relic mass function at redshift  $z = 0$ . Marconi et al. (2004) showed that a good match between the relic and the local BHMFs is obtained for reasonable values of radiative efficiency  $\epsilon_r \sim 0.06 - 0.16$ , Eddington ratios  $\lambda \sim 0.1 - 1.7$  and duty cycles, defined as the ratios of the AGN phases duration at redshift  $z$  to the Hubble time  $t_H(z)$ . Further developments of such studies have been performed in my own Master Thesis and, e. g. in Shankar et al. (2013).

While the evidence for past SMBH accretion episodes and BHs-galaxies interactions is glaring, clear proofs of feedback *in action* onto host galaxies are more difficult to be traced. The effects of the AGN feedback in terms of jets, winds and radiation pressure can both perturbate giant molecular clouds igniting fractioning and intense star formation or conversely shutting it down, if the feedback is powerful enough to swipe gas and dust away from the bulge. This has obviously the consequence to freeze the  $M_{BH}$  to  $M_{bulge}$  ratio.

A robust evidence of *past* feedback processes is observable in the most massive galaxies yet observed, the *Brightest Cluster Galaxies* (BCGs), where a powerful feedback can explain, with gas and dust depletion, the large amount of missing mass with respect to the amount predicted by stellar evolutionary models. Moreover, feedback is able to explain the low star formation rate and the red stellar population in local ellipticals. But proofs of ongoing feedback processes have to be found basically in emission and absorption lines spectroscopy. In Chapter 3 we will explain how delicate is this issue, while Chapter 4 will be dedicated to show observable effects of radiation pressure on broad emission line profiles and, therefore, also on the inferred SMBH masses.

## 1.6 BH mass ladder: BH masses in Active Galactic Nuclei

BH masses in local quiescent galaxies can be measured, as discussed above, by kinematic methods applied on diffuse gas or single stars or even water masers, if present, within the

sphere of influence of the BH. We already pointed out the pros and cons of each technique in Section 1.1. With any of those methods it is quite difficult to estimate BH masses in starburst galaxies and in active nuclei.

First of all, most AGN are so far that the necessary spatial resolution to resolve the sphere of influence is still unachievable. Moreover these kind of sources have so bright nuclei that stellar kinematics or gas spectral features in the host galaxies cannot often be properly evaluated in the observed overall emission.

Indeed, mass measurements are essential for studying the coevolutionary processes of black holes and galaxies and both AGN and starburst phases (which can eventually be ignited by feedback processes during AGN phases or indicate an obscured but still active nucleus) are considered leading actors of such processes. Therefore, it becomes mandatory to include other methods for BH mass estimates. Present mass measurements techniques are here just briefly summarized. For a complete review, we refer to Peterson & Bentz (2011), Peterson (2011) and Shen (2013).

The methods here described define the steps of the so called BH mass ladder Peterson (2004): a sequence of techniques that allows us to estimate masses in ascending order of distance, although often at the expense of time and/or accuracy. The first step in such ladder are of course the stellar and gas kinematical measurements already discussed.

### 1.6.1 Reverberation mapping (RM)

This technique, which represents step number 2 in the BH mass ladder, is based on the assumptions that most of the optical-UV emission from an AGN is due to the accretion disk and that broad emission lines are produced by the fast orbiting clouds of the BLR ionised by the AGN continuum. If this is indeed the case, any fluctuation of the continuum luminosity is then followed by a reverberation at broad lines wavelengths (Blandford & McKee 1982). This echo is emitted with a delay that is quantified by the clouds' distance from the central source and by their position along the orbit and is therefore of the order of  $\frac{r}{c}$ , where  $r$  is the average distance of BLR clouds from the ionising source. Measuring the delay in broad line response gives then a direct estimate of the BLR size (or at least of the average size of the

region producing that particular line). This size,  $r_{line}$ , can then be used to derive the “virial” mass of the BH under the assumption that BLR motions are virialized:

$$M_{BH} = f \frac{(\Delta V)^2 \cdot r_{line}}{G}, \quad (1.4)$$

where  $\Delta V$  is the virial velocity of BLR, assumed to be given by the broad emission line width.  $f$  is factor which takes into account the geometrical and kinematical structure of the BLR.

Although reverberation mapping is usually accounted as a direct method for BH mass measurements, it strongly depends on the factor  $f$ , which is not known. It also assumes, in this simple formulation, that BLR clouds motion is only governed by BH’s gravitational potential, which in turn means that BLR are not sensible to outflows and to radiation pressure. In Chapter 4 we will widely discuss this argument, in order to understand if broad line profiles can hide traces of such processes.

Moreover it is not clear which are the best emission lines to consider and which is the best indicator of the velocity dispersion, whether it is the FWHM or the  $\sigma$  of the broad line. Netzer & Maoz (1990) showed that, in case of a spherical symmetry of the BLR, it should be  $f = \frac{3}{4}$  if we take the FWHM as the dispersion velocity indicator and  $f = 3$  if we choose  $\Delta V = \sigma$  (see, e.g., Kormendy & Ho 2013b). An isotropic distribution of BLR clouds is certainly an oversimplified assumption. Therefore  $f$  becomes a free parameter that has to be observationally constrained. Several attempts have been done in this direction: Woo et al. (2010) have derived an average value of  $\log f = 0.72^{+0.09}_{-0.10}$  by fitting to the observed  $M_{BH} - \sigma_*$  correlation in local quiescent galaxies the predicted relation obtained by using RM masses and  $\sigma_*$  in a subset of AGN for which both the quantities were available. Thus the assumption that both quiescent and active galaxies do follow the same  $M_{BH} - \sigma_*$  relation (Gebhardt et al. 2000b, Greene & Ho 2006) appears to be a fundamental to jump from rod 1 to rod 2 in the BH mass ladder. Another attempt, in order to find reliable average values for  $f$ , takes into account velocity-resolved delay maps (e.g. Bentz et al. 2010; Grier et al. 2013) to build 2D reverberation maps, i.e. reverberation studies as a function of velocity along the line of sight.

Although this is a very promising path, results are only now becoming available due to the difficulties in obtaining datasets of adequate quality.

It is important also to underline that RM is based on broad line observation and it thus reserved to type 1 AGN. Moreover, although the RM technique has no distance limit in principle, the more we increase the redshift the more we select the sources with the highest intrinsic bolometric luminosities and consequently with largest reverberation delays. Moreover, the highest luminosity sources have also the smallest relative variations. RM mass measurements are therefore heavily biased and often require a prohibitive observing time.

### 1.6.2 Single epoch (SE) mass measurements

As already explained above, reverberation mapping machinery is able to provide BH masses only for low redshift active nuclei. The farthest sources studied to the present day is PG 1247+267 with  $z = 2.048$  (Trevese et al. 2014). Including large samples of high redshift quasars is nevertheless fundamental to trace BH accretion through cosmic ages in order to understand the mechanisms of interaction and coevolution with the host galaxies. Eq. 1.4 offers indeed the possibility to estimate masses at all distances and the main issue to be solved is the measurement of the BLR size. Luckily, the latter can be derived through an indirect method involving the observed relation between BLR extension and the luminosity of the continuum emitted by the accretion disk. Kaspi et al. (2000) discovered this relation, by finding  $r_{H\beta} \propto L^{0.70 \pm 0.03}$ . This slope slightly differs from the trivial prediction of  $r \propto L^{0.5}$  and has been later corrected with a larger sample of sources and more accurate measures. A recent update was published by Bentz et al. (2009) and Bentz et al. (2013) who give a slope of  $\alpha = 0.546_{-0.028}^{+0.027}$  (see Figure 1.7).

This relation allows to estimate SMBH mass measurements at any redshift with just single spectra of the AGN: the velocity dispersion is measured by the FWHM or by the  $\sigma$  of a broad line and the continuum luminosity can be derived by fitting the continuum in a featureless spectral window. BH mass is then given by

$$M_{BH} = f \frac{(\Delta V)^2 \cdot k L_{cont}^\alpha}{G}, \quad (1.5)$$

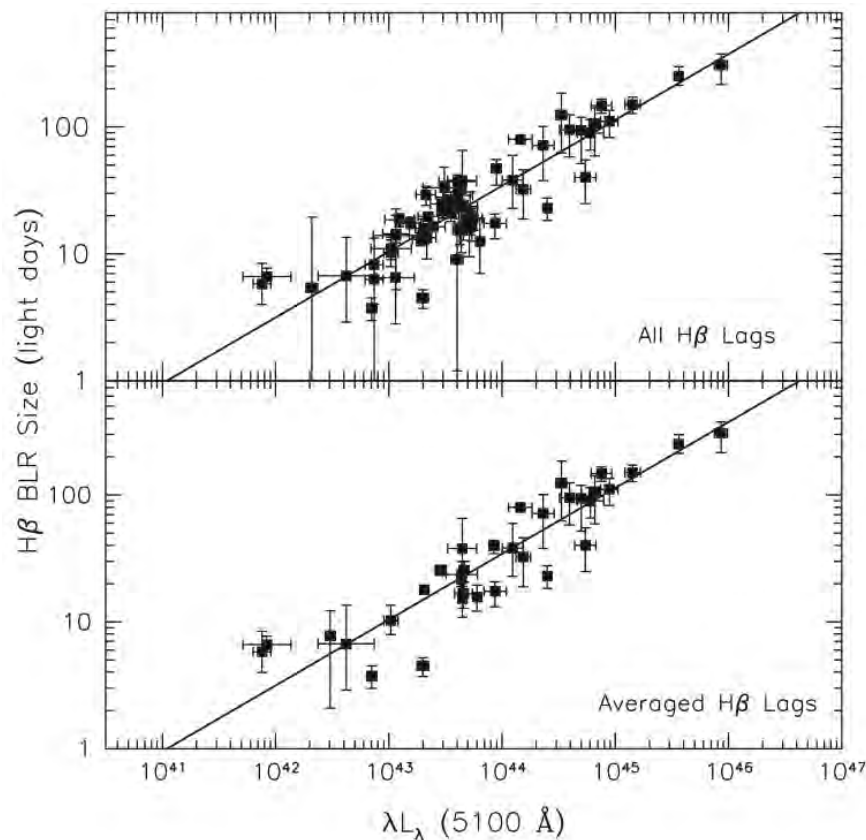


Figure 1.7 The BLR radius-luminosity relation for the  $H\beta$  broad line. *Top* panel show each single data point, while *bottom* panel only shows the weighted mean of multiple measurements for each object.

where  $k$  is the normalization of the BLR size - luminosity relation and  $\alpha$  is its slope. Also  $f$  has to be recalibrated to fit the available RM data and the broad emission line has to be chosen in order to minimize the intrinsic scatter of the radius luminosity relation. In Chapter 2 we will extensively stress this issue by investigating the physical origin of such correlation and deriving indicators the best broad line to be used.

SE masses open the gates to BH demography in large samples. Anyway, since the accuracy of such indirect measurements is lower such that BH masses could be wrong even by a factor of  $\sim 10$ , SE estimates should be only considered from a statistical point of view.

It is also essential to point out that Equation 1.5 does not take into account possible effects of radiation pressure on BLR size. Marconi et al. (2008) showed that ionized BLR clouds are subject to photon momentum deposition and therefore the resultant force is lower than the

one due to the gravitational attraction of the BH. Virial masses are consequently generally underestimated by a factor that strongly depends on the ionizing luminosity produced by the accretion disk and on the average column density of BLR clouds. With this correction term, equation 1.5 assumes the form

$$M_{BH} = f \frac{(\Delta V)^2 \cdot k L_{cont}^\alpha}{G} + g \left[ \frac{\lambda L_\lambda(5100)}{10^{44} \text{erg s}^{-1}} \right], \quad (1.6)$$

where the  $g$  factor has again to be calibrated by imposing the consistency between SE and RM mass measurements. By taking into account this correction factor, the r.m.s. scatter of the ratio of SE to RM mass drops from 0.4 dex to 0.2 dex.

## 1.7 Outline of the thesis

The aim of this thesis is to contribute in building a robust method for SMBH mass measurements to be used in constraining BHs-host galaxies (co)evolution.

As explained above this implies an accurate machinery for deriving BH masses especially at high redshifts. We have explained how, at the present day, only SE mass measurements based on  $M_{BH} - L_{5100}$  correlation can allow us achieve a statistically significant number of masses to be used in SMBH demography studies. Therefore our effort should be addressed to improving SE masses accuracy.

In Chapter 2, we describe the physical origin of the  $M_{BH} - L_{5100}$  relation as a consequence of the structure and emission properties of the BLR, also explaining the role of dust in BLR observational features and deriving a guideline for the choice of the best emission lines for BH mass estimates. Our dynamical model of the BLR also permits to derive predictions about the observed broad emission line profiles. The results presented in Chapter 2 are about to be submitted to the Monthly Notices of the Royal Astronomical Society in the paper “On the physical origin of the radius-luminosity relation in AGNs and the implications for the mass measurements of supermassive black holes” by Sirigu, Marconi et al.

As already mentioned above, broad line profiles and, consequently, SE BH mass estimates

---

can strongly be affected by radiation pressure. The aim of the remaining parts of the thesis is then to unveil the traces of radiation pressure effects on broad lines, if any. Only a very accurate spectral decomposition of a very large sample of sources can reveal traces of significant feedback effects on line profiles.

First of all we require very accurate spectral decomposition and broad line profiles measurements in a large sample of type 1 AGN. In Chapter 3, we consider quasar spectra from the Sloan Digital sky survey data releases 7 and 10 and we present the spectral fitting method, the improvements over previous analysis and the database of broad line widths and continuum luminosities obtained.

Chapter 4 is then dedicated to the results of this extensive spectral fitting, by stressing the effects that radiation pressure has on BH mass estimates and looking for evidences of feedback in action. The results presented in Chapters 3 and 4 are being written on a paper which will be submitted within the first half of next year.

Chapter 5 will summarize our main results and the still open issues.

## **Chapter 2**

# **The physical origin of the radius-luminosity relation in AGN and the implications for the BH mass measurements**

### **2.1 Introduction**

One of the most common signatures of activity in a galactic nucleus is the presence of broad emission lines with Full Width at Half Maximum (FWHM) in the range  $\sim (1 - 20) \times 10^3 \text{ km s}^{-1}$ . These lines are thought to originate in high density gas clouds ionized by the central continuum source and orbiting very close to the massive black hole.

The Broad Line Region (BLR) offers a precious insight into the physical properties of the inner circum-nuclear medium and could shed light on the role of radiation pressure and outflows in the feedback processes which are likely to regulate the coevolution of supermassive black holes (SMBHs) and their host spheroids. BLRs lay deep inside the gravitational spheres of influence of SMBHs and their kinematics is strictly connected to the mass of the black holes. However, BLRs are nowadays still spatially unresolved even in the nearest active nuclei (AGN) and can only be investigated through spectroscopic observations.

Blandford & McKee (1982) first showed how the observed time-resolved variations in broad line profiles are echoes of previous similar fluctuations in the continuum emission from the ionizing source. The time lag can be interpreted as light-travel time between the continuum source and the BLR thus providing an estimate of the BLR size itself. This causal connection can then be used to constrain the enclosed mass of the central source as well, by combining the estimated BLR size with the broad line width  $\Delta V$  as:

$$M_{BH} = f \frac{(\Delta V)^2 R}{G} \quad (2.1)$$

where  $f$  is a parameter determined by the geometry, the orientation and the kinematics of the BLR.

Henceforth, this *reverberation mapping* technique, which in principle has no distance limitation, has been used to estimate BH masses in nearby active galaxies alternatively to spatially resolved kinematical methods (see, e.g., Peterson 2014 and Shen 2013 for recent reviews). However, despite its advantages, reverberation mapping measurements have been performed only on  $\sim 50$  sources due to the extremely large amount of observing time required and, so far, has not been applied to high redshift due to many years long time lag expected (see, e.g., Kaspi et al. 2007). Moreover this technique also suffers from the uncertainty introduced by the unknown scaling factor  $f$ , which can only be calibrated on average by assuming that type 1 AGN follow the same  $M_{BH} - \sigma_*$  relation defined for local quiescent galaxies using spatially resolved gas and star kinematics (see Onken et al. 2004, Woo et al. 2010, Park et al. 2012). Kinematical observations and reverberation mappings thus represent the first two rungs of the so called *black holes mass ladder* (Peterson 2004). A third rung is offered by the observed correlation between the size of the broad-line region and the luminosity of the continuum emission (Kaspi et al. 2000, Kaspi et al. 2005, Bentz et al. 2006b, Bentz et al. 2009, Bentz et al. 2013). Continuum luminosities can thus be used as quick proxies of BLR sizes, providing the so called single epoch (SE) BH mass measurements. This is obviously done at the expense of accuracy although the scatter of the radius-luminosity (hereafter  $R-L$ ) relation seems to be rather small (Wandel et al. 1999, Vestergaard 2002, McLure & Jarvis 2002,

Vestergaard & Peterson 2006, Bentz et al. 2009, Bentz et al. 2013, Peterson 2014).

Some suggestions have been made to explain the origin of the tight  $R-L$  relation mostly assuming that, on average, BLRs have the same physical properties, such as ionization parameter and gas density, thus providing the observed  $R \sim L^{0.5}$  relation (see for example Kaspi et al. 2005, Peterson 2014, Bentz et al. 2013). However, this, like any other “fine tuned” picture of the AGN population, is certainly an oversimplification. The BLR is indeed expected to have a wide range of geometric and physical conditions and it is not clear how this variety is related to the observed small scatter.

The  $R-L$  relation is crucial to compute black holes masses in large samples of sources at all redshifts thus constraining black hole mass functions at different cosmic ages and to remove some of the degeneracies in galaxy evolutionary models and the pathway of massive black hole to the local BH-galaxy relations (see, e.g., the discussion in Lamastra et al. 2010). Recently, the  $R-L$  has also been proposed as a tool to measure accurate luminosity distances of AGN up to  $z \sim 4$  improving the current luminosity distance scale which is so far limited to moderately low redshifts (e.g. Watson et al. 2011). It is therefore very important to understand the effects of geometry, structure and composition on the BLR size in order to explain the physical origin of the  $R-L$  relation and fully exploit its potential.

The work presented in this thesis addresses the issue of the physical origin of the  $R-L$  relation with the help of photoionization models and simple geometrical configurations. The structure and the emission properties of the BLR clouds have been defined by as few free parameters as possible and the parameter space has been explored in order to reproduce the fundamental observed correlation between the mean emissivity radius,  $\bar{R}_{BLR}$ , and the continuum luminosity. In Section 2.2 we describe our BLR model based on single cloud photoionization calculations which are then combined according to the Locally Optimally-emitting Clouds (LOC) model or assuming that Clouds are in Pressure Equilibrium (CPE) with an external confining medium. In Section 2.3 we present the model results on the  $R-L$  relation showing that a boundary for the BLR is needed but that such confinement cannot be provided by dust absorption. In Section 2.4 we discuss the results and propose self-shadowing by BLR clouds as a way to intercept all ionizing photons within the dust

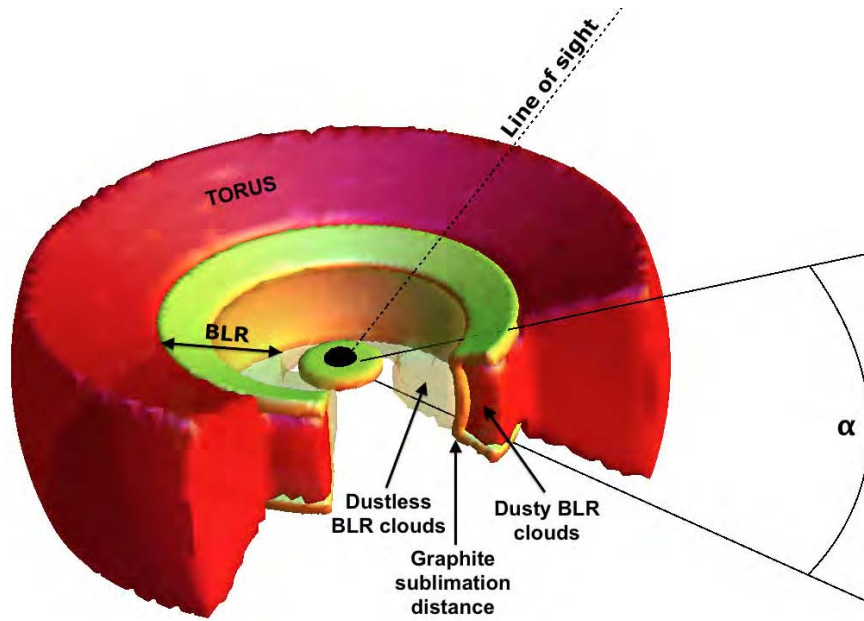


Figure 2.1 Sketch of the *bird's nest* geometry assumed in this thesis in case of presence of a dusty region. In *yellow* the accretion disk surrounding the black hole. BLR dust-free clouds are confined within the *orange* region, while the region in *red* represents where grains may form and/or survive. As we will better explain in the following, the thin *yellow* surface confining dusty BLR clouds represents the *dusty wall*. The angle  $\alpha$  is the aperture of the nest. Sizes in this sketch are obviously *not* in scale.

sublimation radius and we then discuss a possible physical reason why this should happen. In Section 2.5 we show how BH masses can be underestimated if such self-shadowing of BLR clouds does not operate and we finally draw our conclusions in Section 2.6.

We take as a reference the recent determination of the radius-luminosity relation by Bentz et al. (2013) which is valid for the broad  $H\beta$  line:

$$\log\left(\frac{\bar{R}_{BLR}}{1 \text{ lt-day}}\right) = (1.560 \pm 0.024) + (0.546 \pm 0.027) \log\left[\frac{\lambda L_{\lambda}(5100 \text{ \AA})}{10^{44} \text{ erg s}^{-1}}\right] \quad (2.2)$$

here the slope is consistent with the trivial prediction of 0.5.

## 2.2 The Broad Line Region Model

The simple picture we consider for the BLR is that of an axisymmetric disk-like structure rotating around the central SMBH but which can also have an important outflowing component.

This structure is composed of cold ( $T_e \sim 10^4$  K), high density ( $n_e \sim 10^{10} \text{ cm}^{-3}$ ) condensations most of which should be optically thick to ionizing radiation to explain the coexistence of emission lines with a wide range of excitation. These condensations are likely dustless as the BLR sizes inferred from photoionization are usually smaller than the size of the NIR emission region ( $R_{NIR} \sim 0.1$  pc, depending on continuum luminosity), which has been identified with the inner edge of the obscuring torus invoked by the AGN unified model (e.g. Suganuma et al. 2006, Kishimoto et al. 2011). These condensations or clumps are commonly called "clouds" but it is not clear whether they are stably confined or transient structures, steadily formed and dissolved (Netzer & Marziani 2010, Krause et al. 2011).

Recent observational evidence for a flattened structure comes from comparing  $H\beta$ , MgII and CIV equivalent width distributions with that of [OIII] $\lambda$ 5007 in a large sample of quasars from the SDSS (Risaliti et al., 2011). This is just the latest of many suggestions based on many different and independent arguments (Netzer et al. 1992, McLure & Dunlop 2002, Jarvis & McLure 2006, Down et al. 2010, Pancoast et al. 2011, Grier et al. 2013, Pancoast et al. 2014). Conversely, the existence of optically thick clumps rotating around the BH and possibly leaving a cometary trail behind is directly revealed by eclipses of the X-ray source caused by the clumps themselves (Risaliti et al. 2011, Maiolino et al. 2010, Torricelli-Ciamponi et al. 2014); these eclipses and their observed properties confirm that these clumps are BLR clouds with large column densities towards the ionizing source ( $N_H \sim 10^{23} \text{ cm}^{-2}$ ).

It has been proposed that BLR and torus are different parts of the same clumpy structure and they differentiate only for the presence of dust: the clouds within the dust sublimation radius are the BLR while the clouds beyond constitute the putative torus or toroidal obscuring region (Elitzur 2008; Nenkova et al. 2008; Hönic & Kishimoto 2010). Above and below this flattened structure an outflowing wind could exist and could contribute to BLR emission (Elvis 2000, Proga 2007, Elitzur et al. 2014).

Following these observational results and theoretical models, we consider our BLR as made up of clouds in a *bird's nest* configuration (see also Mannucci et al. 1992), shown in Figure 2.1. The red color represent the region beyond the dust sublimation radius where grains can exist, while the orange color denotes the region where dustless BLR clouds are located. We

remark that this configuration is one of many which can explain a series of observations but is not uniquely determined (see, e.g., Goad et al. 2013 for an alternative configuration with a detailed analysis on the inferred observation properties). However, for what concerns the results of this thesis, the only necessary assumption is that there is a continuous distribution of clouds from the inner edge of the BLR to the outer edge of the torus (like, e.g., in Goad et al. 2013).

In order to compute the luminosities of emission lines from the BLR and their spatial distribution, we assume that the clumps encompass a wide range of physical properties, and that the observed luminosities are the sum of the luminosities of the single clumps weighted by some assumed distribution of physical properties.

There are two main classes of photoionization models which take into account the distribution of physical properties of BLR clouds: the Locally Optimally-emitting Clouds (LOC) model (Baldwin et al. 1995) and the Clouds in Pressure Equilibrium (CPE) model (Netzer & Laor 1993). Both LOC and CPE models are described below and will be used to compute emission line fluxes and their dependence with  $r$ , the distance from the central supermassive black hole. In particular, we will use both model classes to estimate the effect of eventual dust grains on the mean emissivity radius. This will be done through the comparison between the  $\bar{R}_{line}$  estimates obtained by considering only the contribution of dust-free clouds and by also including dusty clouds beyond the grains' sublimation limits. Very recently, Baskin et al. (2013) presented a model of a BLR cloud in pressure equilibrium which reproduces many of the observed spectral properties, including the wide range of line excitation. Although this model physically differ from the LOC and CPE ones, which are a superposition of constant density clouds, its predictions for what concern line emission are not very different from LOC a CPE models. Indeed, the single cloud in pressure equilibrium by Baskin et al. (2013) can be reproduced with a suitable distribution of LOC or CPE clouds.

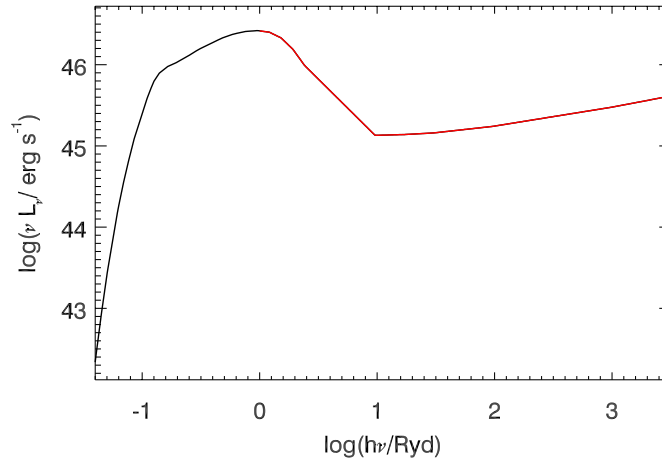


Figure 2.2 Spectral energy distribution of the continuum coming from the accretion disk of the supermassive black hole. In *red* the ionizing portion of the spectrum.

### 2.2.1 Single cloud photoionization models

The emissivity properties of the single clouds are computed with the photoionization code CLOUDY<sup>1</sup> (v. C10.0 and C13.0) developed by Ferland and collaborators (Ferland et al. 1998, Ferland et al. 2013). This photoionization code is able to compute several physical quantities, such as the level of ionization of the gas, the particle density, the kinetic temperature of the gas and the fluxes of about  $10^5$  emission lines. A single cloud model is defined by

- the continuum spectral energy distribution (SED);
- the elemental abundances;
- the ionizing photon flux at the inner surface,  $\phi(r)$ ;
- the constant Hydrogen number density,  $n_H$ ;
- the Hydrogen column density,  $N_H$ .

For ease of comparison, in this thesis we use the same SED used by Mor & Netzer (2012) (Figure 2.2) which, in turn, reproduces the AGN intrinsic spectrum by Marconi et al. (2004).

<sup>1</sup><http://www.nublado.org>

For this SED we have the corresponding bolometric corrections

$$\frac{L_{ion}}{L_{bol}} = 0.50 \quad (2.3)$$

$$\frac{L_{5100}}{L_{bol}} = 0.14 \quad (2.4)$$

where  $L_{5100} = \lambda L_{\lambda}(5100 \text{ \AA})$ . The adopted SED normalization is set to  $\lambda L_{\lambda}(5100 \text{ \AA}) = 10^{46}$  erg/s which corresponds to an ionizing luminosity of  $L_{ion} = 10^{46.57}$  erg/s. However, it should be noted that the models only depend on the ionizing flux and therefore luminosity is just a scaling factor, which allows us to set the size of the cloud and its distance from the ionizing source. Many observations prove that the spectrum can vary with the luminosity of the continuum (see for example Marconi et al. 2004, Lusso et al. 2012, Netzer & Trakhtenbrot 2013). In particular, the spectral index connecting the X-ray and the optical emission is found to become steeper (more negative) with increasing luminosity, as confirmed by many authors (e.g. Vignali et al. 2003b,a, 2005; Strateva et al. 2005; Vasudevan & Fabian 2007). Therefore the assumption of a single template for the SED to be simply normalized to account for different bolometric luminosities does not describe the detail of the observed spectra. However, it is beyond the scope of this thesis to explore the effects of different continuum shapes.

The adopted values for  $\phi$ ,  $n_H$  and  $N_H$  of each cloud of the BLR are then chosen according to the requirement of the class of models (LOC or CPE).

We assume that clouds have elemental abundances which are twice the solar value (Allende Prieto et al. 2001, 2002; Holweger 2001). This is consistent with the absolute abundances measured for Mrk 279 by Arav et al. (2007) and with local quasar average metallicity derived from the N/C ratio by Hamann & Ferland (1992). The adopted values are summarized in the first column of Table 2.1 in the case of dust free gas.

The presence of dust grains, mixed with the gas, is determined by the flux of incident radiation: below a given value, which can be related to a specific distance of the cloud and flux of ionizing radiation by considering the assumed SED, dust grains can survive and are included in the computations unless otherwise specified. We considered two types of spherical dust grains: made of pure graphite or a mixture of graphite and silicates. The corresponding gas

depletions in the two cases are listed in column 2 and 3 of Table 2.1 and, for simplicity, the depletion factors are assumed to be independent on the gas density (see also Spitzer 1985 for comparison). Each grain model is specified by the grain optical properties (the refractive index as a function of photon energy) and the size distribution. In this thesis we assumed the refractive indexes by B. Draine<sup>2</sup> and a size distribution from  $5 \times 10^{-3}$  to  $2.5 \times 10^{-1} \mu\text{m}$  consistent with the one measured in the ISM (see Mathis et al. 1977). Grain opacities are then calculated with CLOUDY following van Hoof et al. (2004). In this thesis we consider only the average grain properties over the entire size distribution. The adopted distribution of grain sizes and the chosen refractive indexes contribute to the inferred absorption and scattering properties of dusty regions. Since such distributions probably vary from one AGN to another, we decided to adopt values which should likely represent the average properties of a large and statistically significant sample of sources. Each grain type is included only in the clouds where the grain temperature is under the sublimation limit for that type<sup>3</sup>. In particular, pure graphite sublimation temperature is set to  $1.75 \times 10^3 \text{ K}$ , while silicates sublimation temperature is set to  $1.40 \times 10^3 \text{ K}$ . These values set the incident radiation flux below which a given grain population can survive and the corresponding sublimation radii are then set by the assumed continuum luminosity. The sublimation radii for graphite and silicate grains are given by Mor & Netzer (2012) and correspond to:

$$R_{graph} \simeq 0.5 \times \left( \frac{L_{bol}}{10^{46} \text{ erg s}^{-1}} \right)^{0.5} \left( \frac{T_{sub}}{1800 \text{ K}} \right)^{-2.8} \text{ pc} \quad (2.5)$$

$$R_{sil} \simeq 1.3 \times \left( \frac{L_{bol}}{10^{46} \text{ erg s}^{-1}} \right)^{0.5} \left( \frac{T_{sub}}{1500 \text{ K}} \right)^{-2.6} \text{ pc} \quad (2.6)$$

The latter expressions give  $R_{graph} = 1.48 \text{ pc}$  in the case of  $L_{ion} = 10^{46.57} \text{ ergs}^{-1}$  and are in very good agreement both with Mor & Netzer (2012) photoionization calculations and with the correlation found by Suganuma et al. (2006) between the size of the NIR emitting region (of the same order of the inner radius of the dusty “torus”) and the luminosity of the continuum. Moreover, for the given  $L_{ion}$  and SED, this value for  $R_{graph}$  can be related to an upper limit

<sup>2</sup><http://www.astro.princeton.edu/~draine/>

<sup>3</sup>CLOUDY does not allow to vary the dust abundance within the clouds. Therefore it is not possible to take into account the possibility that grains might survive deep within the clouds.

Table 2.1 Abundances of elements typically involved in metal depletion due to graphite and silicates grain formation in the ISM.

<b>Element</b>	<b>Dust-free</b> <i>Log(N/N(H))</i>	<b>Graphite</b> <i>Log(N/N(H))</i>	<b>Graphite+Silicates</b> <i>Log(N/N(H))</i>
C	-3.309	-3.707	-3.707
N	-3.769	-3.769	-3.769
O	-3.009	-3.009	-3.231
Na	-5.369	-5.369	-6.068
Mg	-4.159	-4.159	-4.858
Al	-5.229	-5.229	-7.229
Si	-4.159	-4.159	-5.682
S	-4.439	-4.439	-4.439
Ca	-5.339	-5.339	-9.339
Fe	-4.249	-4.249	-6.249
Ni	-5.449	-5.449	-7.449

for the ionizing photon flux  $\phi_{graph} = 10^{18.6} \text{ erg s}^{-1} \text{ cm}^{-2}$ , beyond which graphite grains start to sublimate. In the following we will refer to  $R_{graph}$  and  $\phi_{graph}$  as basis of comparison for discussing our photoionization models results.

### 2.2.2 LOC - Locally Optimally-emitting Clouds

The first class of models we consider is that of Locally Optimally-emitting Clouds (Baldwin et al. 1995). The BLR is represented as a collection of many individual clouds optically thick to ionizing photons. The clouds encompass a large range of physical conditions such that the major contribution to the observable emission is mainly due to those clouds with optimal emission efficiency.

Using SED, elemental abundances and dust grains specified above, all clouds are assumed to have a column density of  $10^{23} \text{ cm}^{-2}$ . Each cloud is then uniquely identified by a specific  $\phi$  and  $n_e$ . We computed a first grid of dust-free models in the ranges  $\log(\phi/\text{s}^{-1} \text{ cm}^{-2}) \in [14, 24]$  and  $\log(n_e/\text{cm}^{-3}) \in [7, 14]$  respectively, with steps of 0.2 dex in each quantity.

If  $C(r)$ ,  $g(n_e)$  and  $h(N_H)$  are, respectively, the covering factor of all clouds at distance  $r$ , the

distribution of hydrogen number and column densities, the line luminosity is then given by

$$\bar{L}_{line} = \iiint \epsilon_{line}(N_H, n_e, r) g(n_e) h(N_H) 4\pi r^2 C(r) dr dn_e dN_H , \quad (2.7)$$

where  $\epsilon_{line}(N_H, n_e, r)$  is the line flux emitted by a single cloud. Clearly, for a given luminosity there is a unique relation between  $r$  and  $\phi(r)$  and the integration on  $r$  can be replaced by an integration over  $\phi(r)$ .

The probability to have a cloud with an electron number density between  $n_e$  and  $n_e + dn_e$  is given by a power-law distribution:

$$g(n_e) \propto n_e^\beta , \quad (2.8)$$

while  $h(N_H)$  is by assumption a Dirac's delta function. The normalization is then

$$\int_{N_{H,min}}^{N_{H,max}} \int_{n_{e,min}}^{n_{e,max}} g(n_e) h(N_H) dn_e dN_H = 1 , \quad (2.9)$$

which in our case is simply

$$\int_{n_{e,min}}^{n_{e,max}} g(n_e) dn_e = 1 \quad (2.10)$$

with  $n_{e,min} = 10^7 \text{ cm}^{-3}$  and  $n_{e,max} = 10^{14} \text{ cm}^{-3}$ . Regarding the covering factor of clouds at distance  $r$ ,  $C(r)$ , we can think of it as made of two contributions. One contribution is given by the solid angle  $\Omega$  which is subtended by the cloud distribution as seen by the central ionizing source. In practice this corresponds to the solid angle identified by angle  $\alpha$  in Figure 2.1. The second contribution is given by  $c(r)$ , the probability that a photon from the central source hits a cloud at distance in the range  $[r, r+dr]$ , once it is emitted within the solid angle  $\Omega$ , that is towards the distribution of clouds. Therefore  $C(r)$  is given by the relation

$$dC(r) = \frac{\Omega}{4\pi} c(r) dr . \quad (2.11)$$

As in typical LOC models,  $C(r)$  and hence  $c(r)$  are given by simple power-laws, so we assume

$$c(r) \propto r^\Gamma \quad (2.12)$$

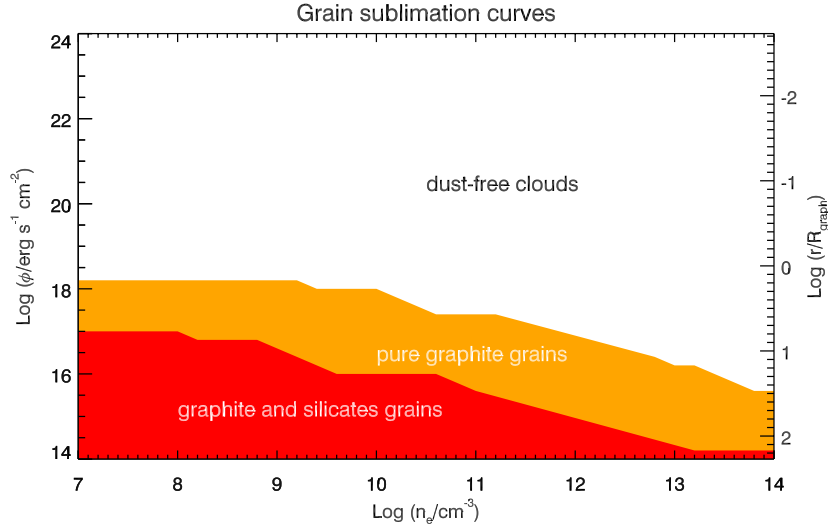


Figure 2.3 Dust sublimation curves. Colored regions represent models with allowed graphite or graphite and silicates grains. The temperature at which each type of dust grains sublimates is also a function of gas density, thus no unique sublimation radius can be provided.

with the normalization condition that

$$\int_{r_{min}}^{r_{max}} c(r) dr = 1 \quad , \quad (2.13)$$

meaning that, at  $r_{max}$ , the probability that an ionizing photon is intercepted by a cloud and hence absorbed is 1. With this formulation we separate the BLR total covering factor, set by  $\Omega/4\pi$ , from the probability that a photon intercepts a cloud;  $r_{max}$  is therefore the maximum distance that an ionizing photon can reach within the clouds' distribution, and we will return to it later.

So far we have not considered the possibility that clouds can shield each other from the ionizing radiation. This effect clearly becomes important close to  $r_{max}$  and can be easily taken into account if the clouds are randomly distributed in space at any given radius. If  $Q(r)$  is the ionizing photon rate reaching the clouds at distance  $r$  the rate of absorbed photons is

$$dQ = -Q(r)c(r)dr \quad (2.14)$$

and this is simply the radiative transfer equation in the absorption case with solution

$$Q(r) = Q_H \exp\left(-\int_{r_{min}}^r c(r')dr'\right) , \quad (2.15)$$

where  $Q_H$  is the total ionizing photon rate that is that seen by clouds at  $r_{min}$ , the inner limit of the BLR. This relation is valid only if the clouds are optically thick to ionizing radiation.

The number of photons absorbed per unit time at distance  $r$  is therefore

$$dQ_{abs}(r) = Q_H \exp\left(-\int_{r_{min}}^r c(r')dr'\right) c(r) dr \quad (2.16)$$

and this equation allows us define the *effective* interception probability per unit distance,  $c_*(r)$ , i.e. the probability for a photon to be intercepted by a cloud at distance  $r$ , taking into account cloud self-shielding:

$$c_*(r) dr = \frac{dQ_{abs}(r)}{Q(r_{min})} = c(r) \exp\left(-\int_{r_{min}}^r c(r')dr'\right) dr . \quad (2.17)$$

We can then define the *effective* total covering factor that takes into account also the effects of clouds' self-shielding, as

$$dC_*(r) = \frac{\Omega}{4\pi} c_*(r) dr . \quad (2.18)$$

The self-shielding of clouds can then be taken into account by using  $c_*(r)$  instead of  $c(r)$  and the normalization condition

$$\int_{r_{min}}^{r_{max}} c_*(r) dr = 1 . \quad (2.19)$$

It should be noted that this correction might be an overestimate because some of the clouds might be only partially absorbing the ionising continuum. This issue will be further discussed in Section 2.4.1.

In order to compute the line profiles as the contribution of all single clouds in the distribution, one needs  $\eta(r)$ , the cloud number density as a function of radius which we assume to be given by a power-law with index  $\epsilon$ :

$$\eta(r) \propto r^\epsilon \quad (2.20)$$

with normalization

$$\int_{r_{min}}^{r_{max}} \eta(r) 4\pi r^2 dr = N , \quad (2.21)$$

where  $N$  is the total number of the clouds. The cross section  $S(r)$  of a cloud at distance  $r$  from the central black hole can be derived from the previous distribution as  $S(r) = c(r)/\eta(r)$ . These quantities can be used to compute mean emissivity weighted radii and dynamic models from which also line profiles can be easily inferred. In particular, the emissivity weighted radius which we use as an estimate of the BLR size to be compared with reverberation mapping results is given by

$$\bar{R}_{line} = \frac{\int_{r_{min}}^{r_{max}} r \cdot r^2 \epsilon_{line}[n_e, \phi(r)] c_*(r) g(n_e) dn_e dr}{\int_{r_{min}}^{r_{max}} r^2 \epsilon_{line}[n_e, \phi(r)] c_*(r) g(n_e) dn_e dr} , \quad (2.22)$$

where we have already used our assumption that the distribution of column density  $h(N_H)$  is a Dirac delta function centered on  $10^{23} \text{ cm}^{-2}$ .

### Grains' sublimation distance in LOC models

For each single cloud in the  $n_e, \phi(r)$  grid we have verified with CLOUDY whether graphite and silicate grains can survive and the results of this exercise are shown in Figure 2.3.

Obviously, the sublimation limits are also a function of gas density, for the grain heating due to collisions with hot electrons. This means that in LOC models, where ionizing photon flux  $\phi$  and electron density  $n_e$  are independent quantities, there is not a unique estimate of dust sublimation distance.

### 2.2.3 CPE - Clouds in Pressure Equilibrium

A different class of models which take into account a distribution in cloud physical properties has been proposed by Netzer and collaborators (e.g. Kaspi & Netzer 1999 and references therein): only single clouds in pressure equilibrium with an external, rarefied and optically thin medium contribute to the observed broad line emissivity, while the others are dispersed

in very short timescale. We refer to such models as *clouds in pressure equilibrium* (CPE) models. So, if we assume that the external pressure, or the magnetic field energy density, varies as a power-law with the distance from the central BH,  $P(r) \propto r^{-s}$ , and we consider that the electron temperature of photoionized clouds is roughly constant, then the electron number density  $n_e$  in each cloud (assumed to be constant within them) has to follow a power-law with the same index:

$$n_e = n_{e,0} \left( \frac{r}{r_0} \right)^{-s} . \quad (2.23)$$

where  $n_{e,0}$  and  $r_0$  set the normalization of electron density and cloud distance, respectively. Following Kaspi & Netzer (1999) we will represent the number of clouds per unit volume as  $N(r) \propto r^{-p}$  and assume that the mass of the clouds is conserved along their orbits.

It is then straightforward to derive all the main geometric and physical conditions of the clouds as simple functions of distance and the two parameters  $s$  and  $p$ . In particular, the cloud column density is given by

$$N_H(r) = N_{H,0} \left( \frac{r}{r_0} \right)^{-\frac{2}{3}s} , \quad (2.24)$$

the cross section of a single cloud by

$$S(r) \propto r^{\frac{2}{3}s} , \quad (2.25)$$

and the covering factor per unit distance by

$$dC(r) \propto r^{\frac{2}{3}s-p} dr . \quad (2.26)$$

In order to consider the effect of self-shielding we have to define, as in the LOC models, the effective covering factor per unit distance as

$$dC_*(r) \propto dC(r) \exp \left( - \int_{r_{min}}^{r_{max}} C(r') dr' \right) dr \quad (2.27)$$

and then take into account the correction factor for the line emission interception probability along the line of sight. The cumulative line luminosity is consequently

$$L_{line} \propto \int_{r_{min}}^{r_{max}} r^2 \epsilon_{line}[N_H(r), n_e(r), \phi(r)] dC_*(r) \quad (2.28)$$

and the mean emissivity radius is given by

$$\bar{R}_{line} = \frac{\int_{r_{min}}^{r_{max}} r \cdot r^2 \epsilon_{line}[N_H(r), n_e(r), \phi(r)] dC_*(r)}{\int_{r_{min}}^{r_{max}} r^2 \epsilon_{line}[N_H(r), n_e(r), \phi(r)] dC_*(r)} \quad (2.29)$$

For each relation, the normalization has been chosen to be consistent with Mor & Netzer (2012), who considered  $n_{e,0} = 10^{9.8} cm^{-3}$  and  $N_{col,0} = 10^{22.66} cm^{-2}$  for an AGN with  $s=1$ ,  $p=1$  and  $\lambda L_\lambda(5100 \text{ \AA}) = 10^{46} erg s^{-1}$ . For clouds' distance we then considered  $r_0 = 10^{18.61} cm$ .

Within the framework just described, we used the same range of cloud distances defined for the LOC models to compute a large amount (1000) of simulated AGN. Each AGN is defined by the continuum ionizing luminosity  $L_{ion}$  and the values of  $s$  and  $p$ . The luminosity, combined with the spectral energy distribution, provides the correspondence between the distances of the clouds and their illuminating ionizing flux  $\phi(r)$ , while the values of  $s$  and  $p$  define the corresponding  $n_e$  and  $N_H$  distributions as functions of clouds' distance. Therefore, for each AGN, the triplet  $(L_{ion}, s, p)$  uniquely identifies an AGN and a curve of cloud models in the  $N_H \otimes n_e \otimes \phi$  space. The parameter space is investigated with a resolution of 0.2 dex bins in each quantity. The two parameters  $s$  and  $p$  are assumed to be normally distributed around the values of 1.25 and 1.5, with an intrinsic dispersion of 0.25 and 0.5 respectively. These values are consistent with Kaspi & Netzer (1999) and are also in accordance with the observations (Rees et al. 1989; Netzer & Marziani 2010). The complete set consists of 1183. These computations also permitted a consistency check between the two photoionization codes CLOUDY (used here) and ION (Netzer 1996, used by Mor & Netzer 2012), by comparing the sublimation limits in the case of  $s = 1$ ,  $p = 1$  and  $\lambda L_\lambda(5100 \text{ \AA}) = 10^{46} erg s^{-1}$ . We notice a very good agreement between the two codes for the expected sublimation radius

of graphite grains: by assuming a spectral energy distribution as in Figure 2.2, normalized to  $\log[\lambda L_\lambda(5100 \text{ \AA})/(\text{erg s}^{-1})] = 10^{46} \text{ erg s}^{-1}$ , Mor & Netzer (2012) give a ION prediction of  $R_{\text{graph}} = 1.32 \text{ pc}$ , while CLOUDY returns  $R_{\text{graph}} = 1.30 \text{ pc}$ .

## 2.3 The radius-luminosity relation: model results

In order to investigate the nature of the correlation between the mean emissivity radius and the luminosity of the continuum, we tested both the LOC and the CPE frameworks in several different physical situations: as a first approach, in Section 2.3.1, we assume the BLR to be completely confined by the dusty region. In this case, only the dust-free clouds contribute to the overall line luminosity and beyond the graphite sublimation limit the clouds are assumed to efficiently absorb all the ionizing photons, thus forming an outer *wall* enclosing the BLR. We will then derive the mean emissivity radius as a function of the model parameters and infer a prediction for a simulated radius-luminosity relation, to be compared with all the observations available to date.

In Section 2.3.3 we present our results for an extended *dust-free* BLR model to show what happens when the BLR is not limited in extension. Even the clouds beyond the sublimation limits will in this case be forced not to host grains up to a very large distance  $r_{\text{max}} \simeq 200R_{\text{graph}}$ . This model might reproduce the situation of rare though existing sources which do not show the typical IR bump due to dust reprocessing of the optical and UV incident photons (Jiang et al. 2010).

In Section 2.3.4, we will present our extended *dusty* models. For such models we will consider the dusty clouds from beyond  $R_{\text{graph}}$  up to  $r_{\text{max}}$ . The inferred mean emissivity radii will be compared with the ones predicted in the case of a dusty wall and in the case of dust-free AGN. This comparison will prove that line suppression due to dust absorption is not sufficient to confine the BLR and that the predicted radius luminosity relation is very similar to the one in the dust-free case.

It is important to remark here that our results in this section are obviously dependent on the upper integration limit  $R_{\text{max}}$ . In the following we will also discuss this dependence but, for

the moment, it is sufficient to anticipate that we selected  $r_{max} \simeq 200R_{graph}$  as roughly the maximum radius at which we can have broad line profiles in sources accreting close to the Eddington luminosity.

### 2.3.1 “Dusty wall” models in the LOC framework

As a first rough approximation, we assume the presence of a *dusty wall* beginning at the graphite sublimation radius, so that the clouds are allowed to contribute to broad line emission only if they lay within this boundary. This latter condition appears to be consistent with the results published by Netzer & Laor (1993) and recently revised by Mor & Netzer (2012) and corresponds to the assumption that, if grains are present, they absorb most of the optical and UV photons, strongly suppressing line emission. In the following sections we will show that, by including dusty clouds contribution to line luminosity, LOC models fail indeed to reproduce a sufficiently strong line suppression due to the presence of high density, low ionization parameter clouds.

In the case of an outer boundary, the integrals in Eq. 2.22 are extended to distances from a certain lower limit (which we set to  $r_{min} = 2.3 \cdot 10^{-3}$  pc) up to the graphite sublimation radius  $R_{graph}$ . Here we set  $R_{graph}$  to the observational constraint published by Suganuma et al. (2006) for the inner radius of the dusty region, thus  $R_{graph} = 1.25$  pc for our assumed continuum luminosity. In the following sections we will also take into account the contribution of clouds with distances up to  $r_{max} \gg R_{graph}$  and check if our prediction for the dust sublimation radius matches the result by Suganuma.

We point out here that in the LOC model the total covering factor  $\Omega/4\pi$  has no influence on the estimation of  $\bar{R}_{line}$ . Moreover, also the slope of  $\eta(r)$  has no relevance for the mean emissivity radii, for it is sufficient to know the total surface covered by clouds as a function of radius and not the number of clouds found at that distance as well. But, as we will discuss in Section 2.5,  $\eta(r)$  is needed for the line profiles computations.

$\bar{R}_{line}$  estimations have been performed for several emission lines, both of high and low ionization. For the purposes of this thesis, we will show our results for  $H\beta$ ,  $MgII\lambda 2798$  and  $CIV\lambda 1549$ . In particular,  $\bar{R}_{H\beta}$  estimates will also prove how it is possible to reproduce the

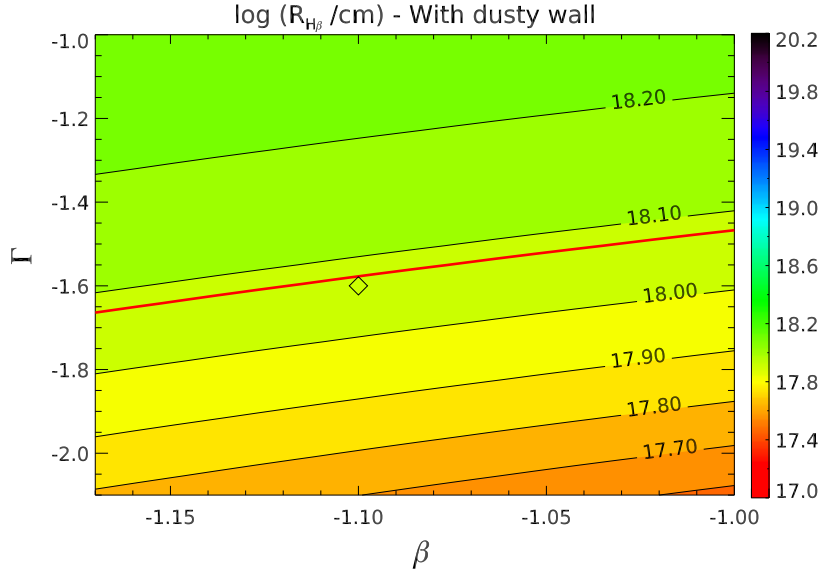


Figure 2.4 BLR mean  $H\beta$  emissivity radii (black contours) as a function of the two indices  $\beta$  and  $\Gamma$  of the density and interception probability distributions respectively, in the case of a dusty shell containing the clouds. The *black* thick contour corresponds to the measure by Bentz et al. (2013), for  $\log[\lambda L_\lambda(5100 \text{ \AA})/(\text{erg s}^{-1})] = 46$ , while the square point is the  $\bar{R}_{H\beta}$  predicted for values of  $\beta$  and  $\Gamma$  typically observed in some previous works (see Nagao et al. 2006).

observed  $R-L$  relation within our parameter space.

### Mean emissivity radii

We performed a first consistency check by verifying that in every cloud model in the ranges  $\log(\phi/s^{-1} \text{cm}^{-2}) \in [18.6, 24]$  and  $\log(n_e/\text{cm}^{-3}) \in [7, 14]$  the dust temperature is above the sublimation limit. This makes us confident that the clouds within  $R_{\text{graph}}$  are actually dust-free ones.

The mean emissivity radius  $\bar{R}_{\text{line}}$  can be computed by following equation 2.22 and is obviously strictly dependent on the values we take for the power law indices defining the structure of BLR clouds,  $\beta$  and  $\Gamma$ . In order reproduce possible physical conditions for sources in a large variety of geometric structures, we summarize in Figure 2.4 our results for the  $H\beta$  line in the ranges  $-1.17 \leq \beta \leq -1$  and  $-2.1 \leq \Gamma \leq -1$ , which are consistent with the observed typical line ratios derived by Nagao et al. (2006) for a large sample of SDSS quasars.

For typical values of  $\beta = -1.1$  and  $\Gamma = -1.6$ , which best reproduce UV line ratios (see Nagao et al. 2006), we obtain a very good agreement with the value predicted by the  $R-L$  relation by Bentz et al. (2013) – see Equation 2.2 – for the broad  $H\beta$  line, with a deviation of less than 0.02 dex.

For comparison, we computed our estimations for  $\bar{R}_{line}$  also in the case of  $MgII\lambda 2798$  and  $CIV\lambda 1549$ . In particular, we can notice that the low ionization  $Mg II$  line (which has a ionization potential of 15.04 eV) is produced more efficiently in a slightly more distant region with respect to  $H\beta$  and the range of  $\bar{R}_{line}$  predicted within the  $\beta-\Gamma$  parameter space is similar to the case of  $H\beta$  line. On the other hand, for higher ionization lines it is expected that most of the emission originates closer to the black hole and that its average radius is more dependent on  $\beta$  and  $\Gamma$  than on the presence of an outer wall. Therefore it is expected that the higher ionization lines, such as  $CIV\lambda 1549$  (which has a ionization potential of 64.49 eV), will span a larger range of  $\bar{R}_{line}$  in the  $\beta-\Gamma$  parameter space. This is indeed what is shown in Figure 2.5.

### The radius-luminosity relation

In order to show the observational implications of our mean emissivity radii estimates, we also used our computations to recreate a *simulated*  $R-L$  relation. We reproduced a large sample of active nuclei (1000), each of which is defined by a bolometric luminosity of the continuum, randomly chosen in the range  $[10^{42.5}; 10^{47}] \text{ erg s}^{-1}$ . The large variety of geometric structures of the sources is represented by different values for  $\beta$  and  $\Gamma$  for each source. Both quantities are considered normally distributed around the standard values of -1.1 and -1.6 respectively and with an intrinsic dispersion of 0.3 dex. The adopted  $\beta$  and  $\Gamma$  distributions give larger ranges than the ones shown in Figures 2.4 and 2.5. For each source the mean emissivity radius is computed, following the Equation 2.22. The results for the  $H\beta$  emission line are presented in Figure 2.6. Obviously,  $H\beta$  radii scale as  $L^{0.5}$  for construction and the luminosity range has been adopted for a comparison with the observed  $R-L$  relation.

The dusty wall model perfectly reproduces BLR sizes in agreement with the Bentz et al.

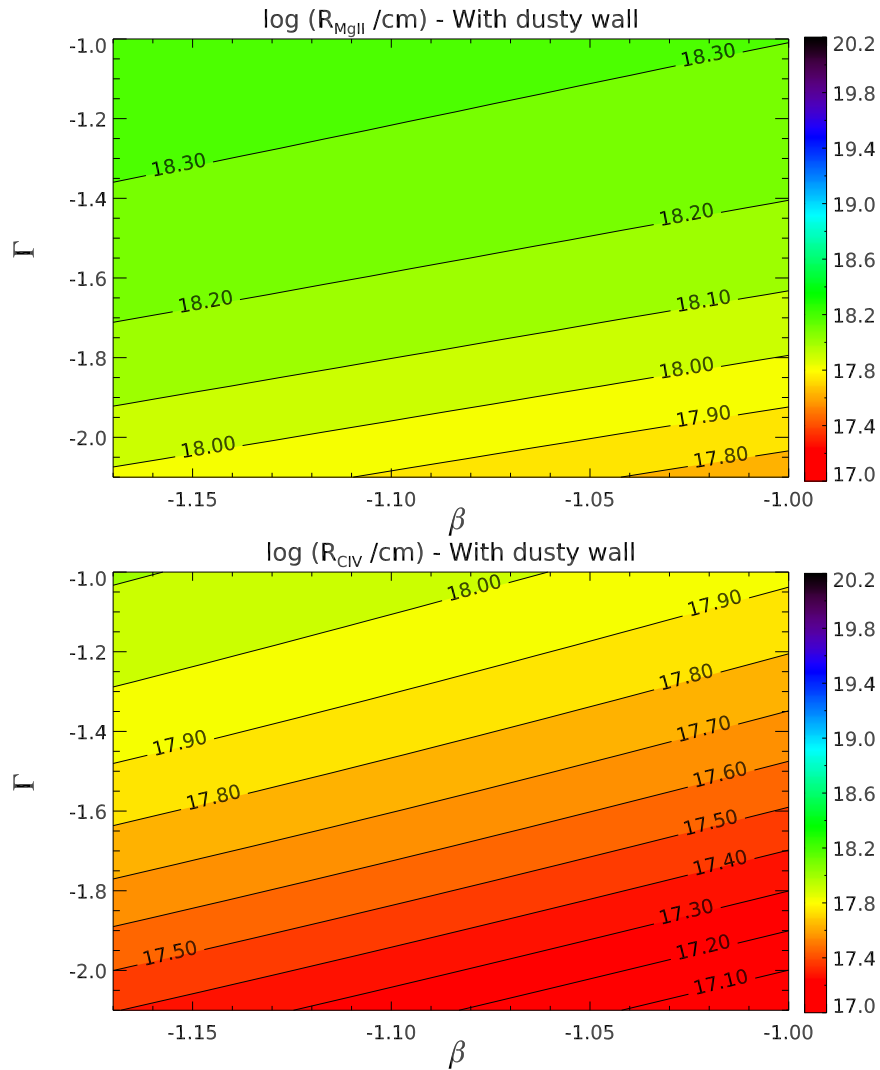


Figure 2.5  $\bar{R}_{line}$  estimates (black contours) for  $MgII\lambda 2798$  (upper panel) and  $CIV\lambda 1549$  (lower panel) in AGN with an external dusty wall containing BLR clouds.  $MgII\lambda 2798$  mean radii within the parameter range are similar to the case of  $H\beta$ , while higher ionization lines, such as  $CIV\lambda 1549$  are produced closer to the BH.

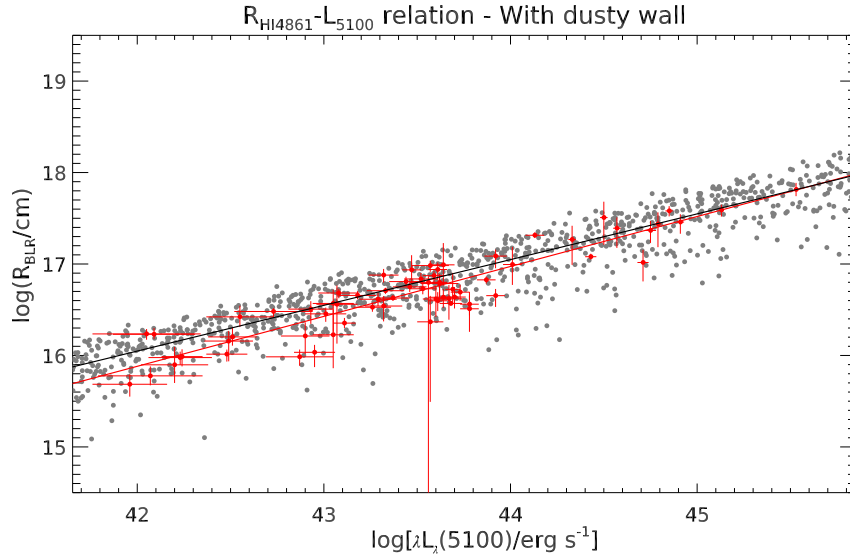


Figure 2.6 Simulated  $R-L$  relation, in the case of dusty wall LOC model for the  $H\beta$  line (*grey* points). All simulated points are our predictions for BLRs with values for  $\beta$  and  $\Gamma$  both distributed according to a Gaussian function around  $-1.1$  and  $-1.6$  respectively, with an intrinsic dispersion of  $0.3$  dex in each case. *Red* points and line show the observations and the radius-luminosity relation by Bentz et al. (2013). The *black* line is our  $R-L$  relation predicted for  $\beta = -1.1$  and  $\Gamma = -1.6$ .

(2013) data at all luminosities and the dispersion of the relation is explained with the distributions of  $\beta$  and  $\Gamma$  defining the structure of the AGN. The asymmetry in the radii distribution for a fixed value of the bolometric luminosity can also be explained by the upper limit imposed by the dusty wall to the distance of the clouds: for a fixed continuum luminosity, the sources with an internal structure resulting in an higher mean emissivity radius are forced to produce the observed line emission within a thinner region approaching the dusty wall. Therefore, the estimated mean emissivity radius distribution is expected to peak close to the dust sublimation distance.

For comparison, we also plot our results for the  $MgII\lambda 2798$  and  $CIV\lambda 1549$  emission in Figure 2.7 (*light brown* - upper panel - and *light green* - lower panel, respectively), while in Figure 2.8 we summarize in histograms all our *dusty wall* models by rescaling the luminosities to a common value of  $\log[\lambda L_\lambda(5100)/(erg s^{-1})]=46$ .

$MgII\lambda 2798$  appears to produce the minimum intrinsic scatter, thus confirming to be one of

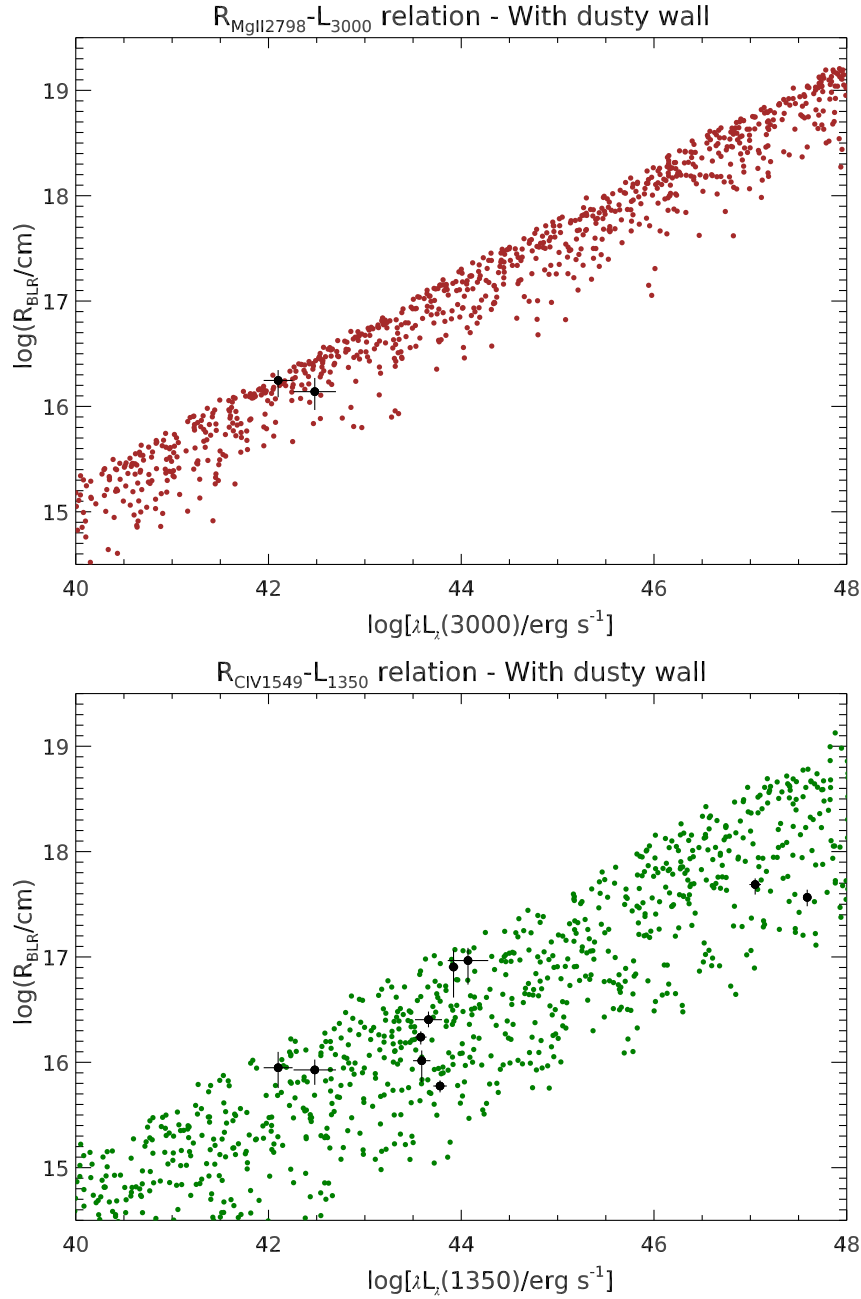


Figure 2.7 Simulated  $R-L$  relations, in the case of dusty sources observed in MgII $\lambda$ 2798 (*upper panel*) and CIV $\lambda$ 1549 (*lower panel*).  $\beta$  and  $\Gamma$  are both distributed according to a Gaussian function around -1.1 and -1.6 respectively with an intrinsic dispersion of 0.3 dex. *Black points* are measures by Metzroth et al. (2006, *upper panel*) and Peterson et al. (2004, 2005, 2014), Metzroth et al. (2006), Kaspi et al. (2007), Trevese et al. (2014) (*lower panel*). In this latter case,  $\lambda L_{\lambda}(5100)$  measures have been converted to  $\lambda L_{\lambda}(1350)$  by assuming a spectral energy distribution as in Figure 2.2.

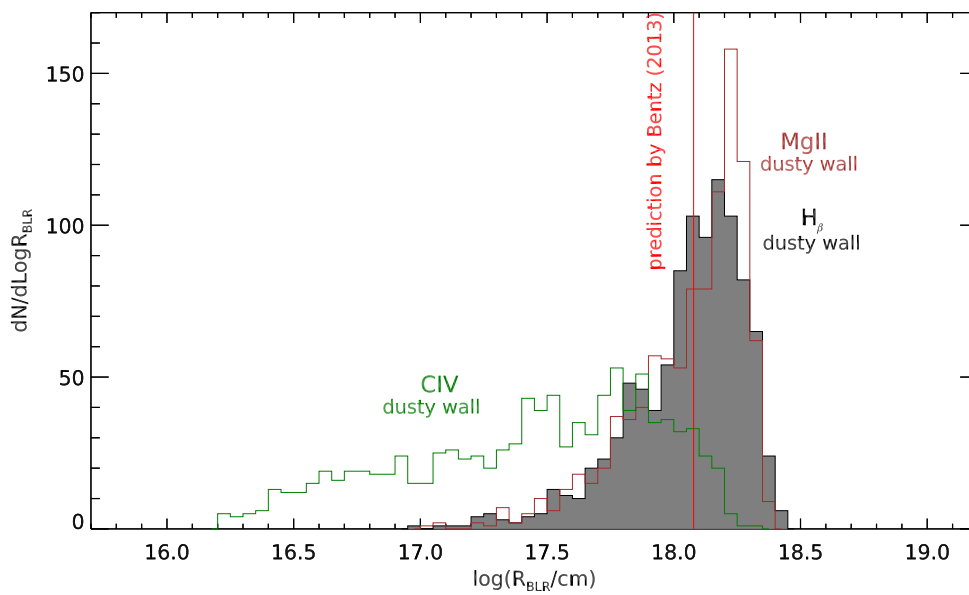


Figure 2.8 Histogram plots of the mean emissivity radii distributions, all rescaled to  $\log[\lambda L_{\lambda}(5100 \text{ \AA}) / (\text{erg s}^{-1})] = 46$ , obtained in dusty wall LOC models for  $H\beta$  (in gray filled),  $\text{MgII}\lambda 2798$  (in brown) and  $\text{CIV}\lambda 1549$  (in green) broad lines, by assuming  $\beta$  and  $\Gamma$  distributed according to a Gaussian function around the values  $-1.1$  and  $-1.6$  respectively and both with an intrinsic dispersion of  $0.3$  dex. The red vertical line shows the prediction of the  $R-L$  relation by Bentz et al. (2013).

the best lines for SE mass estimates, while higher ionization lines such as CIV $\lambda$ 1549 would result in a R-L relation with a huge dispersion, as already anticipated in Section 2.3.1, and thus much less reliable for SE BH mass estimates. For instance, the standard deviations of H $\beta$  and MgII radii for the distributions shown in Figure 2.8 (0.22 dex both) imply an additional scatter of  $\sim 0.3$  dex in  $M_{BH}(H\beta)/M_{BH}(MgII)$  only due to the uncertainties on BLR structure. In the case of SE BH mass measurements derived by the CIV emission line, the standard deviation of CIV $\lambda$ 1549 radii distribution increases to 0.55 dex and the variety of BLR structures is found to contribute to the estimate of the inferred BH masses with an additional scatter of  $\sim 0.6$  dex.

With respect to H $\beta$  broad emission line, as expected, we get a systematic shift of the mean emissivity radii measured: in the case of MgII $\lambda$ 2798 the median of the distribution falls at  $\sim 0.1$  dex larger distances, while for CIV $\lambda$ 1549 we find a difference of  $\sim 0.45$  dex. These results appear to be consistent within the errors with the few reverberation mapping measurements of MgII $\lambda$ 2798 and CIV $\lambda$ 1549 available in the literature (see figure 2.7).

Moreover, if we compare the median of the H $\beta$  distribution in dusty sources with the prediction of the  $R-L$  relation by Bentz et al. (2013) we get a negligible difference of  $\sim 0.02$  dex.

### 2.3.2 “Dusty wall” models in the CPE framework

Very similar results can be obtained by considering the BLR to be correctly described by clouds in pressure equilibrium with the surrounding medium and constrained within an external dusty belt. In this case the mean emissivity radius is given by Equation 2.29.

The variety of possible structures is represented by the distributions of the two parameters  $p$  and  $s$ , both Gaussians centered around 1.5 and 1.25, with intrinsic dispersion of 0.5 and 0.25 respectively. The models within these ranges provide line ratios which are consistent with the observations (e.g., Netzer 2008 and references therein).

In Figure 2.9 we present the simulated radius-luminosity relation for the H $\beta$  line, while in Figure 2.10 we plot our predictions for the Mg II and CIV lines. The distributions are summarized with the histograms in Figure 2.11.

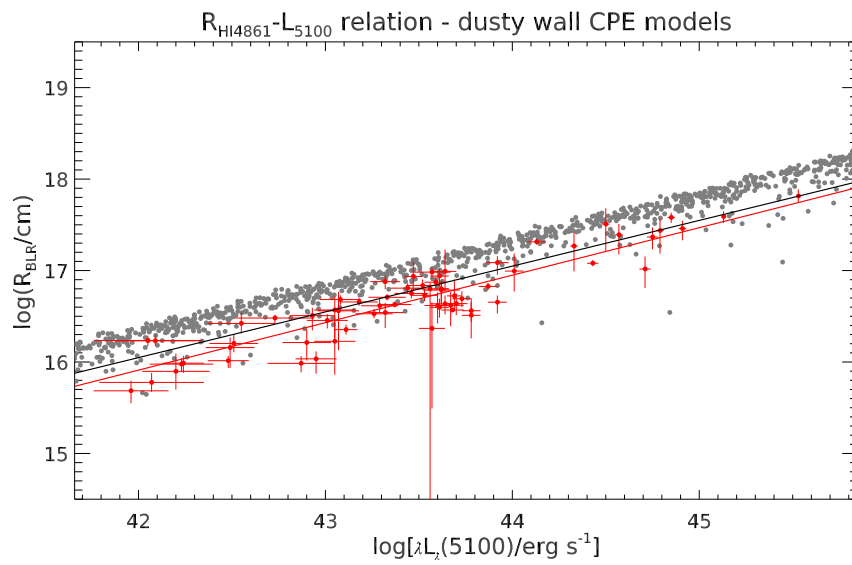


Figure 2.9 Simulated  $R-L$  relation for  $H\beta$ , in the case of a “*dusty wall*” in the CPE framework. The parameters  $p$  and  $s$  are both distributed according to a Gaussian function centered around 1.5 and 1.25, with intrinsic dispersion of 0.5 and 0.25 respectively. *Red* points and line show the observations and the radius-luminosity relation by Bentz et al. (2013). For comparison, the *black* line is our  $R-L$  relation predicted for  $\beta = -1.1$  and  $\Gamma = -1.6$  in the case of the dusty wall LOC model.

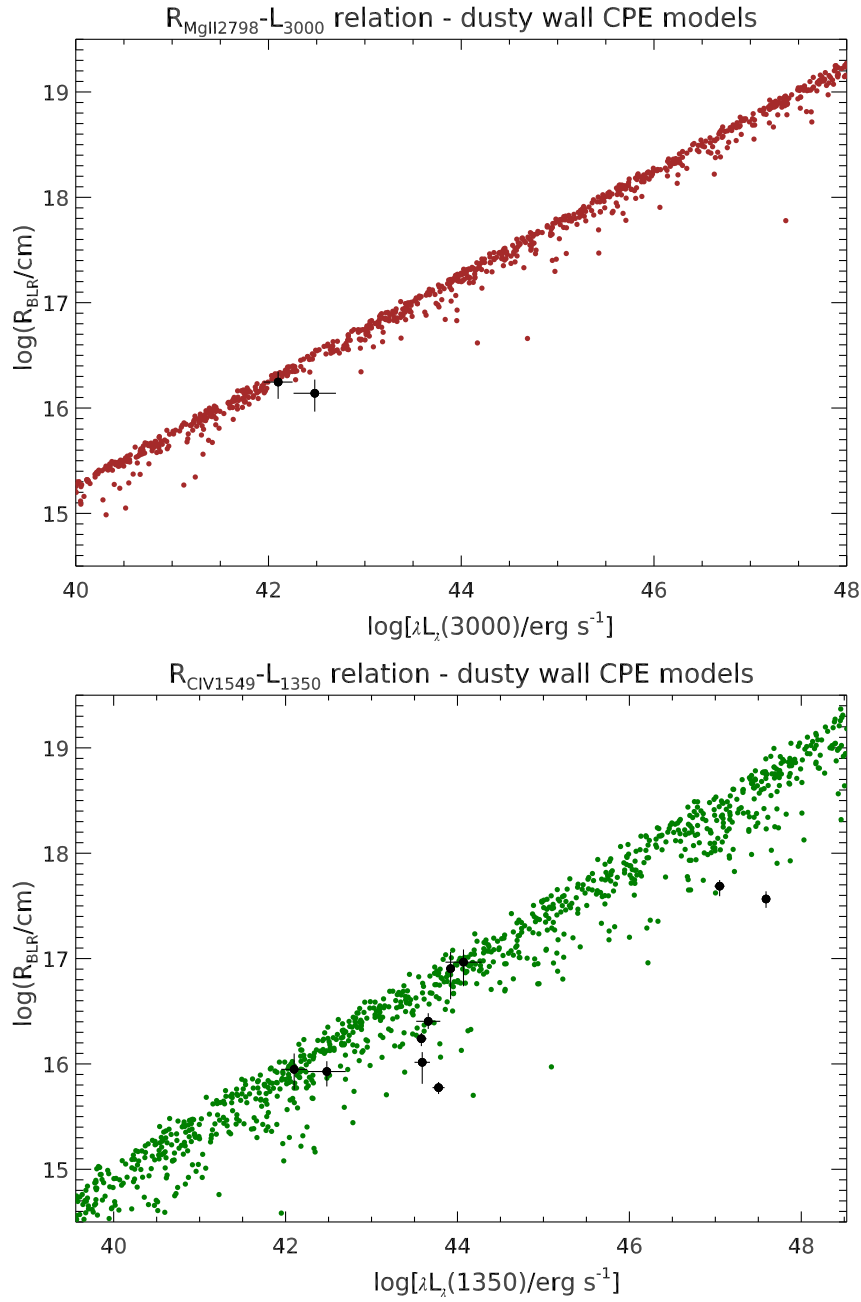


Figure 2.10 Simulated  $R-L$  relation for  $\text{MgII}\lambda 2798$  (upper panel) and  $\text{CIV}\lambda 1549$  (lower panel), in the case of a “dusty wall” in the CPE framework. The parameters  $p$  and  $s$  are both distributed according to a Gaussian function centered around 1.5 and 1.25, with intrinsic dispersion of 0.5 and 0.25 respectively. Black points are measures by Metzroth et al. (2006, upper panel) and Peterson et al. (2004, 2005, 2014), Metzroth et al. (2006), Kaspi et al. (2007), Trevese et al. (2014) (lower panel).

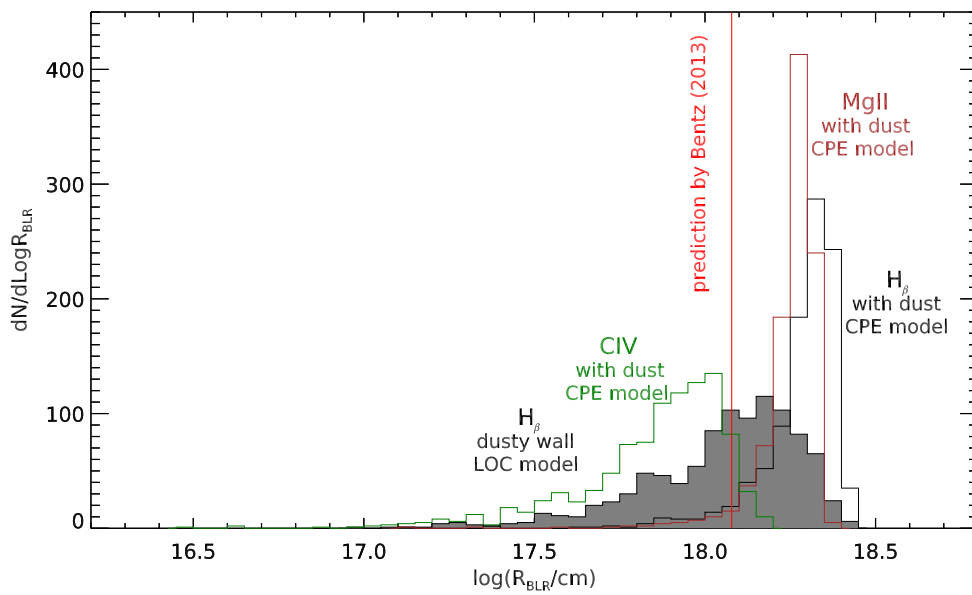


Figure 2.11 Histogram plots of the mean emissivity radii distributions, all rescaled to  $\log[\lambda L_\lambda(5100)/(erg s^{-1})]=46$ , obtained in the CPE framework for  $H\beta$  (in *gray*),  $MgII\lambda 2798$  (in *brown*) and  $CIV\lambda 1549$  (in *green*) broad lines, by assuming  $p$  and  $s$  are both distributed according to a Gaussian function centered around 1.5 and 1.25, with intrinsic dispersion of 0.5 and 0.25 respectively. For comparison, in *gray filled* we show the same  $H\beta$  histogram of Figure 2.8, corresponding to the dusty wall LOC model. The *red* vertical line shows the prediction of the  $R-L$  relation by Bentz et al. (2013) for the  $H\beta$  broad line.

Our computations show an extremely sharp distribution of the  $H\beta$  distribution and an even lower dispersion for the Mg II emission line.

### 2.3.3 The extended *dust free* models in the LOC framework

If, for any reason, the formation of grains in the circumnuclear region is prevented or has not yet taken place, or even if the dust once formed has been swept away, the BLR emission is expected to extend far beyond  $R_{graph}$ . In the outer region, the clouds could still have a ionization parameter high enough to let them contribute significantly to the broad line emission. This would result in an increased measure of the mean emissivity radius. We will reproduce the physical conditions in such sources by also considering the contribution of purely gaseous clouds down to  $\log(\phi/s^{-1}cm^{-2}) = 14$ , corresponding to  $r = 2.4 \times 10^4$  light days, i.e.  $\sim 200 R_{graph}$ . In the following, we will refer to such sources as to “dust-free” AGN. These kind of sources can resemble the physical structure of hot-dust-poor quasars (HDP), first detected in X-ray selected type 1 AGN and later confirmed also at in optical/IR selected quasar samples (Hao et al. 2010, 2011; Jun & Im 2013). The fraction of HDP appears to be strongly dependent on redshift, going from 6% at  $z < 2$  to 20% at  $2 < z < 3.5$  (Hao et al. 2010). Dust-poor sources have also been detected up to  $z \sim 6$  (Jiang et al. 2010).

#### Mean emissivity radii

In Figure 2.12 (*upper* panel) we show our results for the mean emissivity radius derived from the  $H\beta$  line, as a function of the two parameters  $\beta$  and  $\Gamma$ . It is clearly visible that the photoionization calculations perfectly reproduce the effect of an increased mean emissivity radius: given, for example,  $\beta = -1.1$  and  $\Gamma = -1.6$ ,  $\bar{R}_{H\beta}$  is increased by factor of  $\sim 1.2$  dex with respect to the estimates in the dusty wall model.

Moreover, we derive from these models that the lack of a dusty wall allows the size of the BLR to be extremely dependent on the indices that describe the distribution of the clouds. In such dust-free AGN, the mean emissivity radii span, in the same parameter space, a range about 100 times larger with respect to dusty sources (see Figure 2.4). As we will better

explain in Section 2.4 and 2.5, this effect makes BH mass measurements in the case of extended BLRs even more difficult and unreliable.

### The radius-luminosity relation

For a direct comparison, we add in Figure 2.14 (*dark blue* points) our computation for the  $H\beta$  simulated R-L relation (the corresponding histograms are shown in *black* in Figure 2.16). It is straightforward to notice the serious overestimation of BLR sizes at all luminosities, due to the added contribution of dust-free clouds beyond the sublimation distance. Moreover, the mean emissivity radii estimates appear to be extremely sensible to the value of the structural parameters  $\beta$  and  $\Gamma$ , thus resulting in a huge dispersion of the radii distribution for a given specific continuum luminosity. In other words, the “dusty wall” we previously considered has the function of letting the mean observable properties of the BLRs to be almost independent on the intrinsic structural distributions of the clouds. If this outer boundary is not there, the geometry of the system prevails and broadens the R-L observed relation.

In the following we will show that no significant differences from this scenario are introduced by including dust in the outer clouds.

### 2.3.4 Extended *dusty* models in the LOC framework

In order to check if LOC models are able to reproduce the sublimation radius predicted by Suganuma et al. (2006) and the effect of an efficient dust absorption beyond  $R_{graph}$ , we repeated our computations by allowing dust grains to survive at distances for which temperature is below the sublimation limit and extending cloud contribution to line luminosity up to the distance of  $R_{max} = 200R_{graph}$ .

#### Mean emissivity radii

The mean emissivity radii as a function of  $\beta$  and  $\Gamma$  predicted by our extended dusty LOC models are presented in Figure 2.12 (*lower panel*) for the  $H\beta$  line and in Figure 2.13 for Mg II and C IV lines.

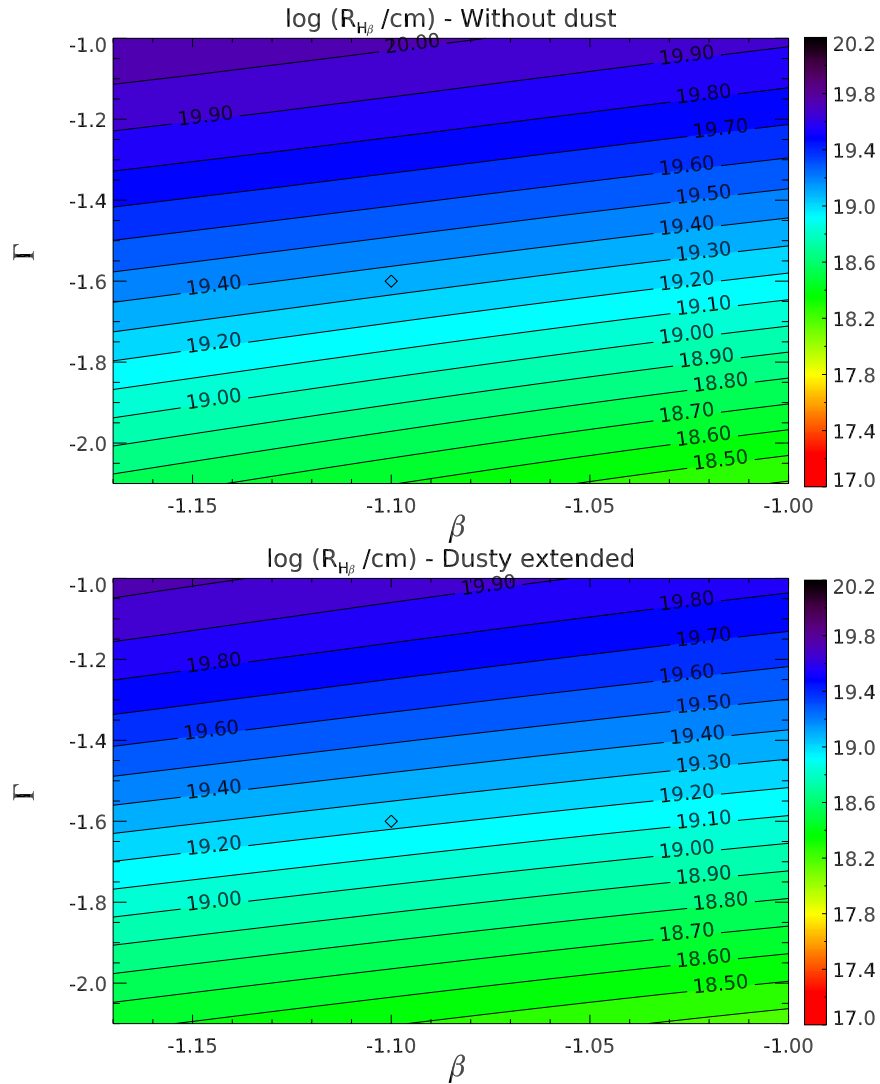


Figure 2.12 BLR mean  $H_{\beta}$  emissivity radii as a function of the two indices  $\beta$  and  $\Gamma$  of the density and interception probability distributions respectively, in the case of absence of dust grains and an external belt confining the BLR. Over the same parameter space, the predicted radii span a much larger range and, for given values of  $\beta$  and  $\Gamma$ ,  $R_{H\beta}$  is typically increased by a factor of  $\sim 1.2$  dex with respect to the estimates in the dusty wall model.

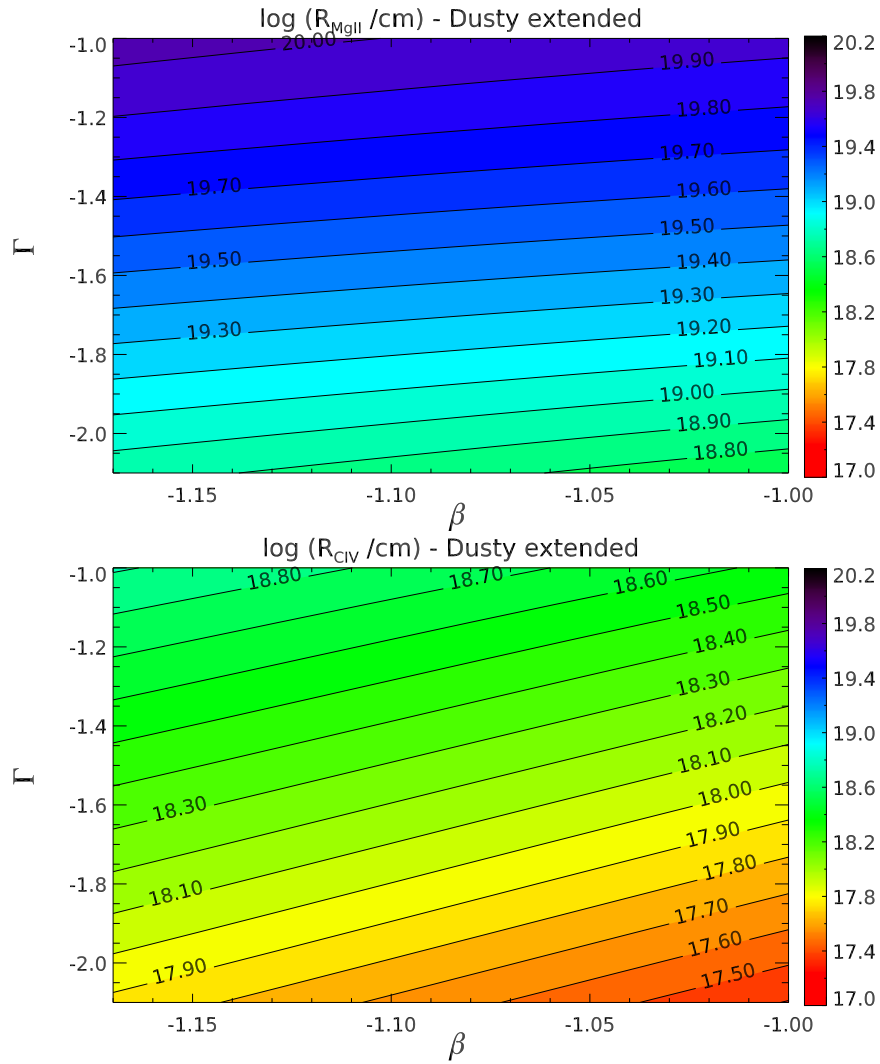


Figure 2.13 Mean emissivity radii for  $\text{MgII}\lambda 2798$  (upper panel) and  $\text{CIV}\lambda 1549$  (lower panel) broad lines as a function of the two indices  $\beta$  and  $\Gamma$  of the density and interception probability distributions respectively, in the case of dusty extended BLRs. Over the same parameter space, the predicted radii span a much larger range and, for given values of  $\beta$  and  $\Gamma$ ,  $\bar{R}_{H\beta}$  is typically increased by a factor of  $\sim 1.2$  dex with respect to the estimates in the dusty wall model.

By comparing the two panels in Figure 2.12 it is clearly visible that no large variations are inferred by adding dust in the clouds beyond the sublimation limits. Both extended models - with and without dust grains - give  $\bar{R}_{H\beta}$  significantly larger than the prediction by Bentz et al. (2013). As we will better explain also in Section 2.4, this has to be ascribed to the weak effect of dust absorption on the overall broad line luminosity. These results lead us to a first important conclusion: *there must be a physical reason, in addition to dust absorption, for the mean emissivity radius of dusty AGN to be so close to the one derived with the simplified model of the dusty wall.* In the following Section 2.3.5 we will also prove that this result is not due to the LOC approach, but is also found with a completely different description of BLR clouds' properties.

### The radius-luminosity relation

For a direct comparison between our results for the radius-luminosity relation in the two cases of the extended BLR LOC models (with and without dust grains within the clouds), we present our prediction for the R-L relation in Figure 2.14 and 2.15, for the  $H\beta$ , Mg II and C IV emission lines respectively. The corresponding histograms are shown in Figure 2.16. It is clearly visible how the two extended LOC models (with and without dust grains beyond the sublimation distances) span almost exactly the same region in the radius-luminosity plane, thus indicating that dust absorption is not sufficient to explain the confinement of the line emitting region.

### 2.3.5 Extended *dusty* models in the CPE framework

In Figures 2.17 and 2.18 we present our results for the simulated R-L relations based on CPE models in the three cases of the broad  $H\beta$ , Mg II and C IV emission lines.

It is clearly visible a systematic shift of the predicted mean emissivity radii at every luminosity, with respect to the expected relation by Bentz et al. (2013). The dispersion of the relations is still high if compared with the case of the simple dusty wall LOC model, but is certainly lower than the one predicted with the extended LOC models (see Figure 2.14).

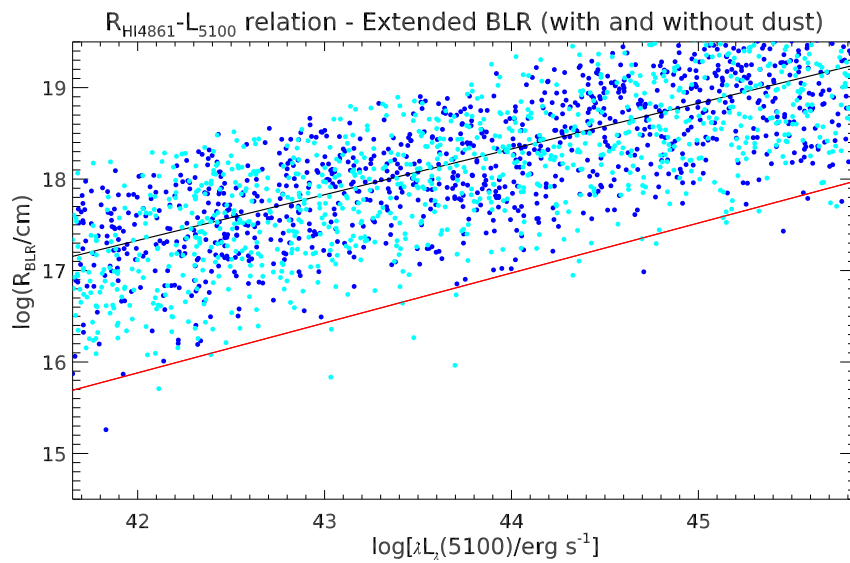


Figure 2.14 Simulated  $R-L$  relation for the  $H\beta$  line, in the case of the extended LOC model with (*azure* points) or without (*blue* points) dust grains beyond the sublimation limits. Again,  $\beta$  and  $\Gamma$  are both distributed according to a Gaussian function around  $-1.1$  and  $-1.6$  respectively, with an intrinsic dispersion of  $0.3$  dex in each case. *Red* line shows the radius-luminosity relation by Bentz et al. (2013), while the *black* line represents the R-L relation for dusty extended BLR in the case of  $\beta = -1.1$  and  $\Gamma = -1.6$ .

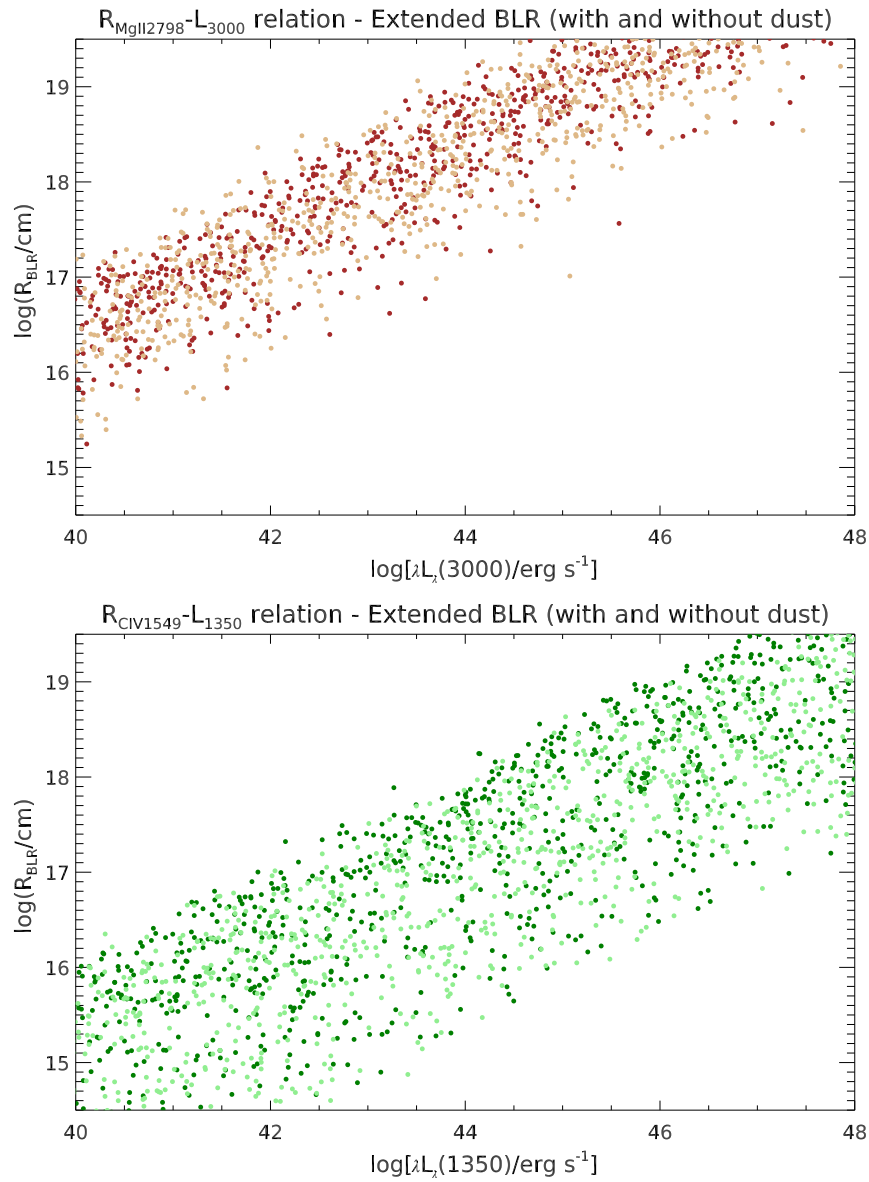


Figure 2.15 Simulated  $R-L$  relation for  $\text{MgII}\lambda 2798$  (*upper panel*) and  $\text{CIV}\lambda 1549$  (*lower panel*), in the case of the LOC model by including or not dust grains (*light and dark colors*, respectively) beyond the sublimation limits.  $\beta$  and  $\Gamma$  are both distributed according to a Gaussian function around -1.1 and -1.6 respectively, with an intrinsic dispersion of 0.3 dex in each case.

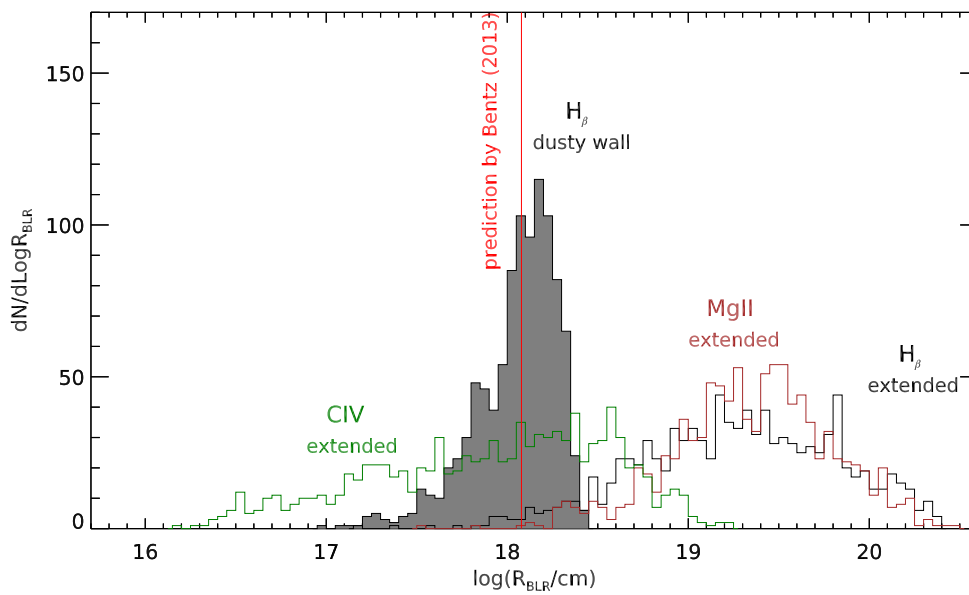


Figure 2.16 Histogram plots of the mean emissivity radii distributions, all rescaled to  $\log[\lambda L_\lambda(5100)]/(erg\ s^{-1})=46$ , obtained for  $H\beta$  broad line in dusty wall (in *gray filled*) and extended dusty LOC models for the  $H\beta$  (in *black*),  $Mg\text{II}\lambda 2798$  (in *brown*) and  $C\text{IV}\lambda 1549$  (in *green*) broad lines, by assuming  $\beta$  and  $\Gamma$  both distributed according to a Gaussian function around the values  $-1.1$  and  $-1.6$  respectively and both with an intrinsic dispersion of  $0.3$  dex. The *red* vertical line shows the prediction of the  $R-L$  relation by Bentz et al. (2013) for the  $H\beta$  emission line.

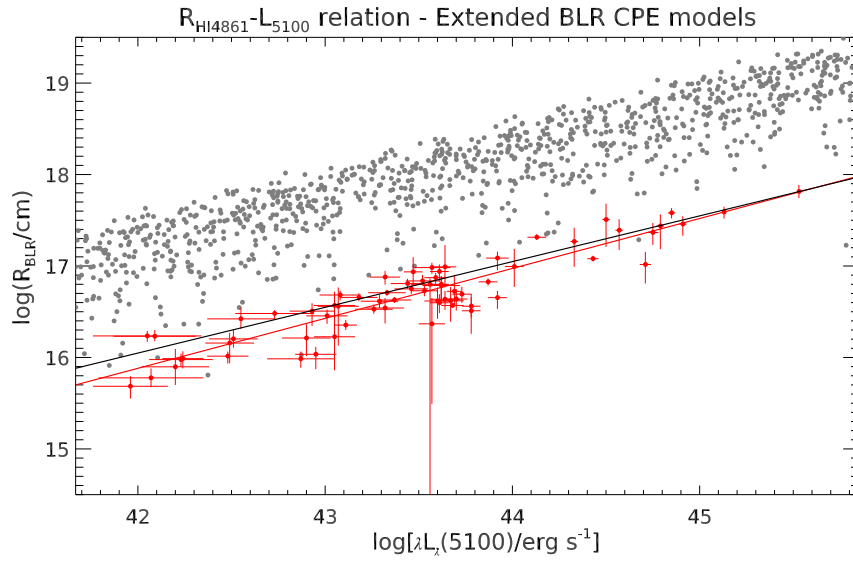


Figure 2.17 *Gray* points represent the simulated  $R-L$  relation, in the case of the dusty extended CPE models for the  $H\beta$  broad emission line.  $\beta$  and  $\Gamma$  are both distributed according to a Gaussian function around  $-1.1$  and  $-1.6$  respectively with an intrinsic dispersion of  $0.3$  dex. *Red* points and line show the observations and the radius-luminosity relation by Bentz et al. (2013). The *black* line is our  $R-L$  relation predicted for  $\beta = -1.1$  and  $\Gamma = -1.6$  in the case of the dusty wall LOC model.

This is better shown with the histograms in Figure 2.19: the median of the  $H\beta$  CPE model distribution is  $\sim 1.3$  dex higher than expected, and its standard deviation is  $\sim 1.7$  times the one obtained for the dusty wall LOC model.

The systematic shift in mean emissivity radii, which is consistent with the case of extended LOC models, means that average values of the mean emissivity radii do not depend on the chosen approach to describe the distributions of the clouds: both models fail to reproduce correctly the expected  $R-L$  relation because of the insufficient suppression of the overall line emissivity by dust grains beyond the sublimation limits.

## 2.4 The origin of the radius-luminosity relation

The photoionization calculations presented in the previous sections have shown that if we consider an external boundary of the order of  $R_{graph}$  for emitting BLR clouds (i) mean emis-

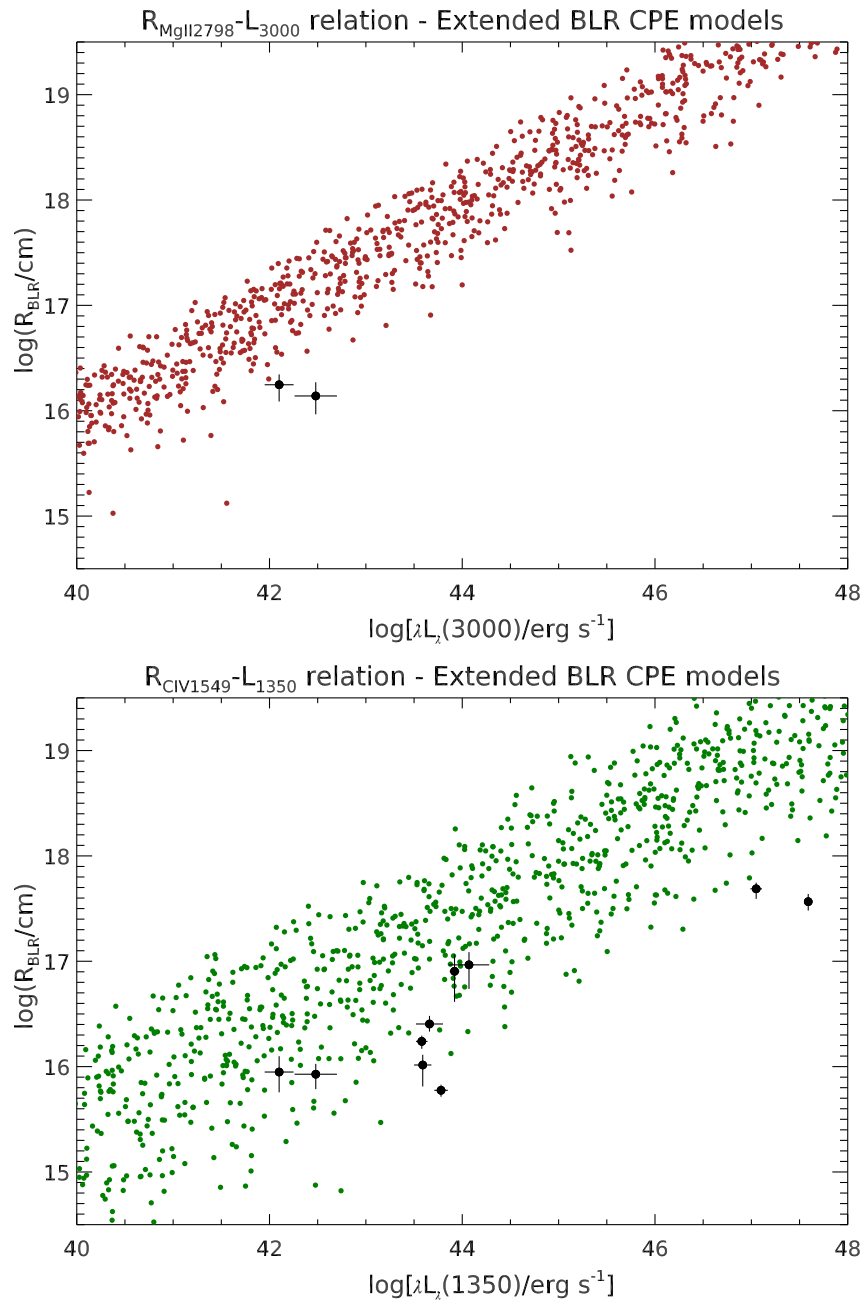


Figure 2.18 Simulated  $R-L$  relations, in the case of a extended CPE models for the  $\text{MgII}\lambda 2798$  (*upper panel*) and  $\text{CIV}\lambda 1549$  (*lower panel*) emission lines. In this latter case,  $\lambda L_{\lambda}(5100)$  measures have been converted to  $\lambda L_{\lambda}(1350)$  by assuming a spectral energy distribution as in Figure 2.2.  $\beta$  and  $\Gamma$  are both distributed according to a Gaussian function around  $-1.1$  and  $-1.6$  respectively with an intrinsic dispersion of  $0.3$  dex. *Black* points are measures by Metzroth et al. (2006, *upper panel*) and Peterson et al. (2004, 2005, 2014), Metzroth et al. (2006), Kaspi et al. (2007), Trevese et al. (2014) (*lower panel*).

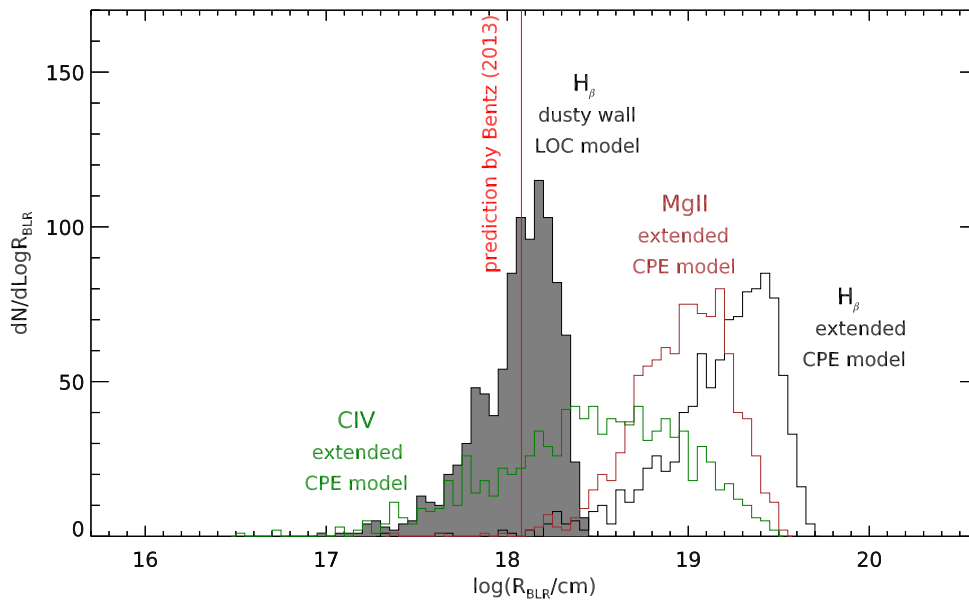


Figure 2.19 Histogram plots of the mean emissivity radii distributions, all rescaled to  $\log[\lambda L_{\lambda}(5100)/(erg s^{-1})]=46$ , obtained in the CPE framework for  $H\beta$  (in *gray*),  $Mg_{II}\lambda 2798$  (in *brown*) and  $CIV\lambda 1549$  (in *green*) broad lines, by assuming  $\beta$  and  $\Gamma$  distributed according to a Gaussian function around the values  $-1.1$  and  $-1.6$  respectively and both with an intrinsic dispersion of  $0.3$  dex. For comparison, in *gray filled* we show the  $H\beta$  histogram corresponding to the dusty wall LOC model. The *red* vertical line shows the prediction of the  $R-L$  relation by Bentz et al. (2013) for the  $H\beta$  broad line.

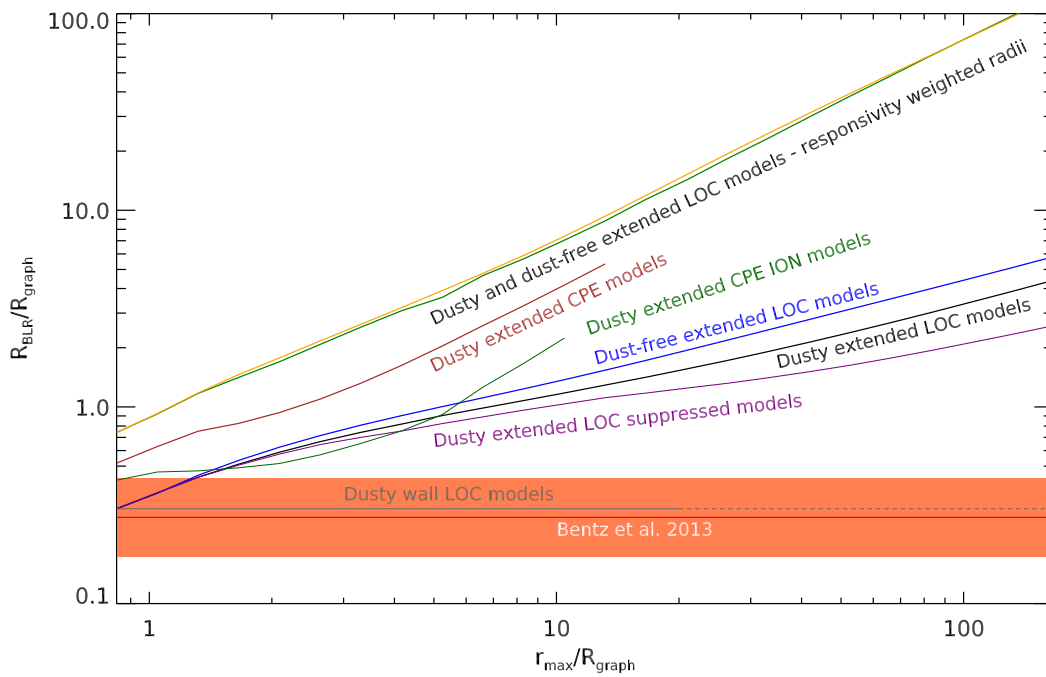


Figure 2.20 BLR mean emissivity radius as a function of the upper integration limit. Both quantities are expressed in units of  $R_{graph}$ . Gray line corresponds to the simple “dusty wall” LOC model; for comparison red line and the orange region represent the estimate by Bentz et al. (2013) with a relative error bar; black and blue line are for dusty and dust-free LOC extended models respectively and green and yellow curves show the prediction for mean responsivity weighted radii in the two cases of dusty and dust-free sources respectively. We also add, in brown and dark green the CPE models, computed with CLOUDY and ION respectively.

sivity radii are consistent with observations and (ii) their dependence on the intrinsic cloud distribution is greatly reduced, thus accounting for the observed scatter of the  $R-L$  relation. In other words, *it is the existence of this sharp outer boundary that ultimately defines the normalization and small scatter observed in the radius-luminosity relation.*

However, the results of our dusty extended models have clearly shown that dust absorption of ionizing photons is not efficient enough to provide the required outer boundary of the BLR. This effect is larger for the LOC models where in the high density clouds at low ionization parameter the gas wins the competition with dust for the absorption of ionizing photons. Overall, the presence of dust does not produce a significant suppression of line emission, as confirmed by the comparison with the dustless extended models. As a consequence, the absence of an external boundary is responsible for the large dependence of the mean emissivity radius on the assumed cloud distribution and increases the intrinsic dispersion of the  $R-L$  correlation.

More quantitatively, it is clear that only the distribution of radii relative to the “*dusty wall*” model is centered around the mean radius predicted by Bentz et al. (2013) for the given continuum luminosity, with a scatter of just  $\sim 0.07$  dex in the case of the LOC models, which is a fair match of the observed dispersion of the data. Both dusty and dustless extended models provide larger emissivity radii: the two distributions have median values which are 1.1 and 1.2 dex larger than that the dusty wall model, regardless of the framework (LOC or CPE) we adopt to describe the distribution of clouds’ physical properties.

It is important here also to point out that no significant effects are obtained by including observational constraints for the extended models: for instance, by excluding those models for which line ratios are not consistent with the what observed in SDSS quasars (e.g. Nagao et al. 2006), we have no significant deviation from the  $R-L$  relations presented.

So far we considered extended models with a very large outer radius ( $R_{max} = 200R_{graph}$ ) and the resulting discrepancy between the predicted and observed  $R-L$  relations might be ascribed to this choice. In figure 2.20 we plot the mean emissivity radius as a function of  $r_{max}$ , for a given bolometric luminosity of the continuum and for the different frameworks considered (LOC or CPE). The desired effect of an outer BLR boundary causing suppression

of line emission would be that the BLR size becomes almost independent of  $r_{max}$  for a relatively wide range of  $r_{max}$  values. This is not the case for any of the extended BLR models we have considered: the dust-free extended LOC models (blue line, see Sec. 2.3.3), the dusty extended LOC models (gray line, see Sec. 2.3.4), the dusty extended CPE models (brown models, see Sec. 2.3.5). All the above models were computed using CLOUDY, therefore we also considered the results of the dusty extended CPE models computed with ION by Mor & Netzer (2012, green line). In case that the suppression of line emission computed by CLOUDY in the dusty models is somewhat underestimated, we have manually suppressed the emergent line fluxes by a factor of 7 for all the CPE cloud models which include dust grains (violet line). This factor is estimated in order to match the gap found by Mor & Netzer (2012) for  $H\beta$  line emissivity at the graphite grains sublimation distance. Even this artificial line suppression is not enough to provide the desired effect of BLR size independent of  $r_{max}$ . We also tested whether the above results might change when considering a different estimate of the BLR size, like the responsivity weighted radius (see Korista & Goad 2004 and references therein). As shown by the yellow and green lines in the figure, the dust does not significantly affect the BLR size which, again, increases quite steeply with  $r_{max}$ .

The lesson learned from Figure 2.20 is therefore that the outer boundary of the BLR cannot be provided by dust and that there must be another physical effect that efficiently confines the BLR emitting region within a distance of the order of  $R_{graph}$ , which is needed in order to explain magnitude and scatter of the observed radius-luminosity relation.

The understanding of the physical origin of the BLR can then be translated into understanding the physical reason why BLR line emission should be confined with  $\sim R_{graph}$ , with no appreciable contribution from dust absorption of ionizing photons. One possible suggestion might come from the true meaning of the quantity  $r_{max}$  which is not simply the maximum distance allowed for the clouds, but the distance at which the probability that ionizing photons intercept a cloud reaches one. Beyond  $r_{max}$  we do not have cloud contribution to the total line luminosity just because beyond that limit clouds are shielded by the inner ones and no ionizing photons reach them. Therefore, the problem can be reduced to explain why all ionizing photons have to be absorbed within  $\sim R_{graph}$ .

### 2.4.1 Possible scenarios

We summarise here the physical reasons why there should be no line emission beyond  $R_{graph}$ . We recall that the absorption of ionizing photons by dust and the corresponding suppression of line emission is not efficient for dense gas clouds with low ionization parameter, i.e.  $\log U \lesssim -1$ , where the gas optical depth to ionizing photons is larger than that of dust. The simplest explanation is therefore the absence of gas clouds with low ionization parameter beyond  $R_{graph}$ : clouds with densities  $\log(n_H/\text{cm}^3) \gtrsim 7-8$  should not exist beyond  $R_{graph}$ . We find no physical reason why that should happen in all AGN.

A simple explanation could be that emission lines beyond  $R_{graph}$  are suppressed because line photons do not escape: the AGN continuum ionizes the dense gas clouds beyond  $R_{graph}$ , emission lines are produced but their photons are intercepted by another dusty cloud within the torus where they are absorbed by dust. In this case line emission can come only from the outer layers of the obscuring torus even from distances larger than  $R_{graph}$ , if the torus geometry is appropriate (see, e.g., the one in Goad et al. 2013). The emission region beyond  $R_{graph}$  must in any case be negligible compared to the one from the dustless clouds.

Another possible simple physical explanation is provided by figure 2.21 where we show the fraction of ionizing photons which is transmitted by a single cloud as a function of ionizing photon flux and gas density. These fraction values are estimated by simply comparing the ionizing flux illuminating the exposed cloud surface with the transmitted one provided by CLOUDY, not including the diffuse emission from the cloud.

The blue and purple colors represent clouds which transmit more than 70% of the incident photons, while for orange and red colors the transmission fraction drops to less than 30%. It can be easily recognised that the clouds with lower optical depth to ionizing photons are those with high ionization parameter ( $\log U \gg -1$ ) and represent the hot phase in the thermally unstable region of the  $n_H - \Phi$  plane (see, e.g., Krolik et al. 1981). Conversely, all clouds with  $\log U < -1$  are optically thick to ionizing photons, thus they can effectively block all the photons along the lines of sight where they are located.

Let us then consider one possible distribution of clouds locations (i.e.  $\Phi$ ) and densities

( $n_H$ ). It is clear from figure 2.21 that, e.g., only the clouds with  $\log(n_H/\text{cm}^3) \gtrsim 12.5$  at  $\log(\Phi/\text{s}^{-1}) \sim 22$  will block all incident ionizing photons, while the majority of clouds in the range  $\log(n_H/\text{cm}^3) \sim 7 - 12.5$  will be optically thin: at the distance corresponding to  $\log(\Phi/\text{s}^{-1}) \sim 22$  the majority of clouds will be optically thin. Conversely, at distances of the order of the dust sublimation radius, any cloud in the density range considered will be optically thick. Therefore, it is highly likely that all ionizing photons will be intercepted at distances which are, at most, of the order of  $\sim R_{graph}$ ; this fact effectively creates the “wall” at  $\sim R_{graph}$  required to explain the observed properties of the  $R-L$  relation. In practice, this explanation requires that all directions from the region emitting ionizing photons to the volume occupied by the BLR are filled with gas  $\log(n_H/\text{cm}^3) > 7$  by  $\sim R_{graph}$ . If this is not the case, the photons will not be blocked, will reach the dense gas clouds beyond  $R_{graph}$  and will generate an oversized BLR, compared to the expectations of the  $R-L$  relation. One of the consequences of this scenario is that virial BH masses will be grossly underestimated as explained in the next section.

The diagram shown in figure 2.21 consider clouds with column densities of  $N_H = 10^{23} \text{ cm}^{-2}$  but the results for clouds with low ionization parameter ( $\log U < -1$ ) does not depend on the clouds column density, provided that they are radiation bound. We can estimate the minimum column density of a cloud to be radiation bounded as a function of the cloud ionization parameter as follows. If a cloud can be approximated as a thin spherical layer at radius  $R$  with covering factor  $\Omega$  we write the equilibrium condition to be radiation bounded, i.e. that the rate of ionizing photons hitting the cloud is equal to the number of recombinations within the cloud:

$$Q(H) \frac{\Omega}{4\pi} = n_e n(H) \alpha_B(H, T_e) \Omega R^2 dR \quad (2.30)$$

with the column density  $N_H = n(H) dR$  we can finally write

$$N_H = \frac{Q(H)}{4\pi R^2 n_e c} \frac{c}{\alpha_B(H, T_e)} = U \frac{c}{\alpha_B(H, T_e)} \simeq 1.2 \times 10^{22} \text{ cm}^{-2} \left( \frac{U}{0.1} \right) \quad (2.31)$$

where we have used  $\alpha_B(H, T_e) = 2.6 \times 10^{-13} \text{ cm}^3 \text{ s}^{-1}$  as suitable for  $T_e = 10^4$  K. Therefore, when a cloud has a low ionization parameter ( $\log U < -1$ ), it will intercept all the photons if

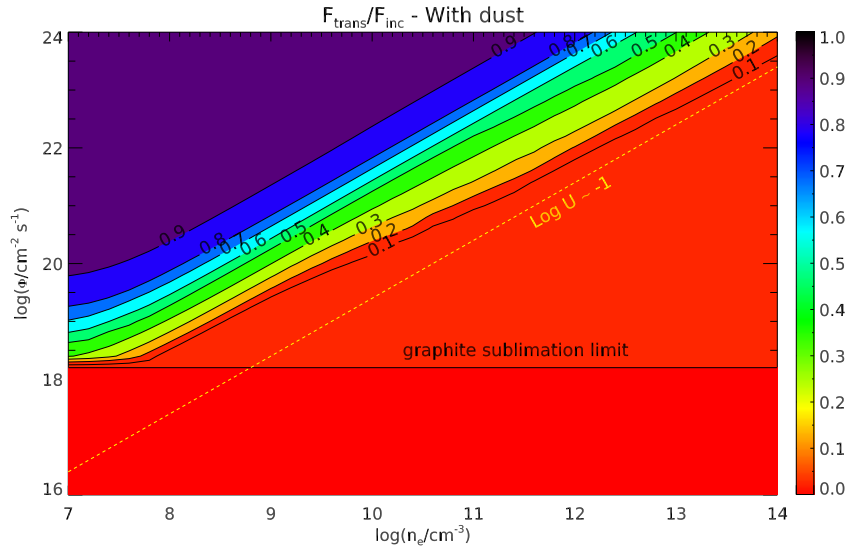


Figure 2.21 Fraction of transmitted ionizing radiation through BLR clouds, computed with CLOUDY, as a function of cloud density and ionizing flux. With decreasing ionization parameter the fraction rapidly drops. The dashed *yellow* line represents  $\text{Log } U = -1$ .

it has a column density of at least  $\sim 10^{22} \text{ cm}^{-2}$ .

In conclusion, the simple scenario just presented supports the presence of three distinct components in the BLR structure. A first component is represented by the highly ionized optically thin clouds within  $R_{\text{graph}}$ , the second is given by the optically thick dusty clouds of the “wall” at  $\sim R_{\text{graph}}$  and the third component is represented by the optically thick dusty clouds close to the plane of symmetry and shielded from ionizing radiation. Only the first two layers can contribute efficiently to the observed line emission while the latter region plays indeed the role of an inner offshoot of the “torus”.

This model would also naturally explain why the observational evidences of a Lyman absorption edge are very rare (Maiolino et al. 2001) and naturally solves the issue of where is the line emission from the inner boundary of the torus.

## 2.5 Line profiles and black hole mass measurements

The consequences of BLR structure and emission properties on the measured line widths and the inferred SE black hole mass measurements have been investigated by computing

emission line profiles.

In particular, we consider the consequences on line profiles and virial BH masses in the case the “dusty wall” is not effective in suppressing line emission.

To derive line profiles we assumed a dynamic model for the clouds: each cloud will follow, on first approximation, a circular orbit around the central supermassive black hole, with a maximum inclination of  $\alpha/2$  with respect to the plane of the accretion disk (see Figure 2.1). The gravitational interactions and the viscosity between the clouds have been modeled with a weak additional turbulence, parameterised with a random velocity component. Outflows and inflows are in this simple case excluded.

Each line emitted by a cloud is assumed to have a Gaussian profile due to its thermal velocity distribution and is Doppler-shifted by a wavelength  $\Delta\lambda$  depending on the projection of the total velocity of the cloud along the line of sight. The total line profile is then given by the superposition of the many contributions by the single clouds.

The profiles obviously depend on the assumed values for  $\beta$ ,  $\Gamma$  and  $\epsilon$ , on the mass of the black hole and on the ionizing luminosity. They also depend on the aperture of the nest, on the line of sight inclination with respect to the plane of symmetry of the system and on the relevance of the turbulent motion. A full analysis will soon be published in a forthcoming paper, while in this thesis we only remark the effects of line quenching by a physical constrain on the distances of BLR efficiently emitting clouds.

If, for example, we consider the framework of LOC models and assume to have a black hole of mass  $10^9 M_\odot$ , a continuum luminosity such that  $\log[\lambda L_\lambda(5100 \text{ \AA})/(\text{erg s}^{-1})]=46$ , standard values for the indices  $\beta = -1.1$  and  $\Gamma = -1.6$ , an aperture of the nest of  $\alpha = 60^\circ$  and a turbulence of about  $500 \text{ km s}^{-1}$ , we get, for an inclination angle of  $10^\circ$ , the profiles plotted in Figure 2.22, in the two cases of a AGN with an external dusty wall (*black* profile) and an AGN without an external boundary to BLR clouds (*blue* profile). In the latter case, we are neglecting the effect of the galactic potential to the line width. It is clear that if the contribution to line luminosity of the farthest clouds is suppressed for the covering factor reaching unity at distances of the same order of graphite sublimation limit, the consequent relative contribution of high velocity clouds is more relevant, thus increasing the measured

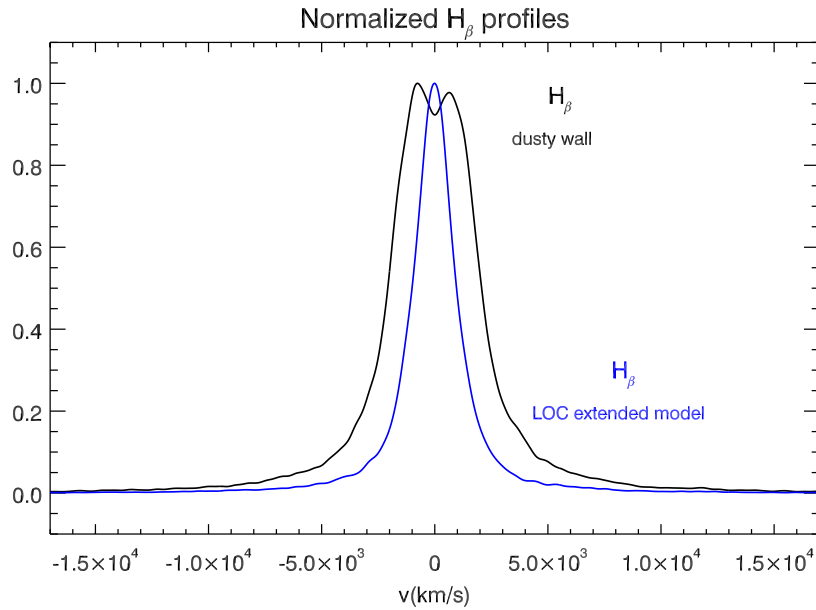


Figure 2.22 Comparison between the  $H\beta$  normalized profiles in dusty wall (in *black*) and dusty extended (in *blue*) LOC models. The effect of the outer boundary is to confine the clouds in a smaller region, increasing the relative contribution of high velocity clouds to the profile. The line width in dust-free sources is therefore expected to be smaller. The smoothness of the profiles is governed by the slope of  $\eta(r)$ , set in this example to  $-2.5$ .

line width. The main implication is that overlooking the important effect on the emission line profiles of an outer boundary for the efficiently emitting BLR clouds, means to relentlessly underestimate SE black hole masses. Using, for instance, the calibration by Vestergaard & Peterson (2006) we obtain in our case an SE inferred mass of just  $\sim 10^{8.2} M_{\odot}$  compared to the assumed  $M_{BH} = 10^9 M_{\odot}$ . In particular, we derived from our simulations that the possible underestimations of the black hole masses in extended BLR models can reach even  $\sim 2$  dex (see Figure 2.23).

The effect just described might be the origin of apparently low BH masses in some sources like Narrow Line Seyfert 1 galaxies (e.g., Peterson 2011) or dustless high redshift quasars (e.g. Jiang et al. 2010); in the latter case line photons are not absorbed by the dusty clouds in the torus and gas clouds might be sparse enough that ionizing photons reach well beyond  $R_{graph}$ .

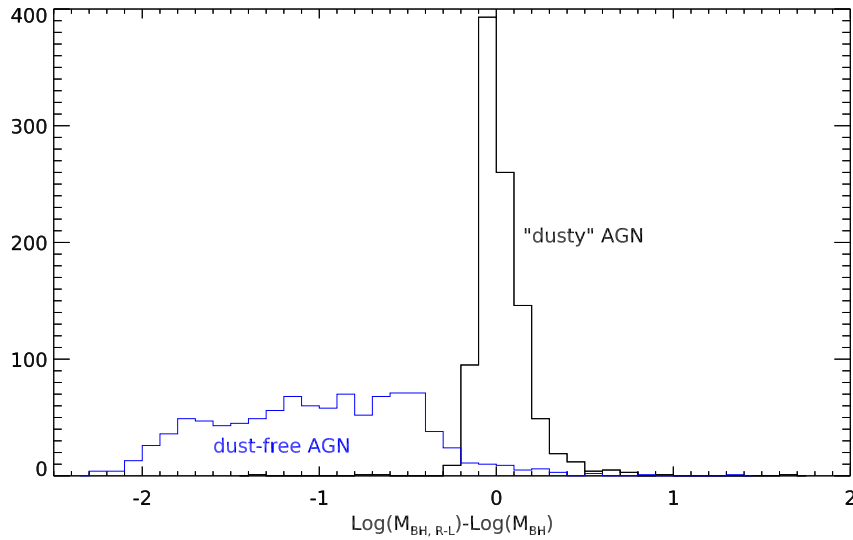


Figure 2.23 Differences (in log scale) between the mass derived by standard R-L relation and the true mass of the black hole. The set of 1000 black holes is defined by  $L$  randomly chosen in the range  $[10^{43}, 10^{45}] \text{ erg s}^{-1}$  and  $\beta$  and  $\Gamma$  both distributed according to a Gaussian function around -1.1 and -1.6 respectively with an intrinsic scatter of 0.3 dex each. In *black*, AGN with a dusty wall confining the BLR (consistent with the calibration of the *observed* R-L relation) and in *blue* extended sources, for which the observed R-L relation is inappropriately used.

## 2.6 Conclusions

We computed photoionization models of the BLR to study the origin of the correlation between the size of the broad-line region and the continuum luminosity observed in broad-line AGN.

We showed how a well-defined outer boundary of the BLR is needed in order to explain the observed  $R-L$  relation, and that the maximum distance of clouds significantly contributing to the broad-line luminosity has to be of the same order of magnitude as  $R_{graph}$ . We also proved that these conclusions are not dependent on the photoionization code used for our computations and on the chosen approach to describe the physical properties of BLR clouds. We also showed that dust cannot be responsible for the existence of such physical limit and, indeed, if we consider also the contribution of clouds far beyond  $R_{graph}$ , very large BLR sizes are expected giving rise to a R-L relation with much larger normalization and intrinsic dispersion than expected. Incidentally, in any source with a significant contribution of broad line emission beyond  $R_{graph}$ , virial BH masses can be underestimated by a factor up to  $\sim 100$ .

One possibility to explain the observed  $R-L$  relation is that all ionizing photons are intercepted by BLR clouds and absorbed within  $\sim R_{graph}$ . Thus any cloud beyond  $\sim R_{graph}$  would be shielded from the clouds closer in and would not emit line radiation. This could happen because at  $\sim R_{graph}$  all gas clouds with densities in the range  $10^9 - 10^{14} \text{ cm}^{-3}$  become optically thick to ionizing radiation suggesting that the probability of intercepting an ionizing photon goes rapidly to 1.

If the proposed picture for the origin of the  $R-L$  relation is correct, then the dusty torus would be heated only by non-ionizing radiation and the BLR would effectively constitute the inner face of the torus, absorbing all ionizing photons.

## **Chapter 3**

# **Spectral fitting of SDSS DR7 and DR10**

## **Quasars**

### **3.1 Introduction**

As already mentioned in Chapter 1, the effort in trying to reproduce SMBHs evolution and unveiling BHs-galaxies interactions requires a very large sample of sources, as unbiased as possible, in order to test the orientation-based explanation of the observed phenomenology and understand how an AGN phase starts, evolves and ends. A large number of BH masses in a wide redshift range can in turn be used to select the theoretical evolutionary accretion scenarios which best reproduce the observations.

Active galactic nuclei appear as spatially resolved objects only with very high spatial resolution observations and in the nearby universe, thus implying that the traces of nuclear activity have to be detected, in the vast majority of cases, through their spectral features and their light curve variability. AGN detection surveys have therefore to face two main issues: collect enough light from the farthest and faintest objects in the deep sky and rule out stellar contaminations from the sample.

Since the first radio surveys, the detection and selection techniques used for the active nuclei census has followed step by step the discovery of their peculiar emission properties. Only since the formulation of a unifying theory the crucial issues of biases and completeness of

the samples reached a leading role in determining the observational and theoretical criteria for planning and elaborating surveys. The orientation of the AGN with respect to the line of sight, the presence of dust, an eventual high emission from starbursts or the presence of unusual types of stars are all factors that definitely complicate the identifications of nuclear activity by masking specific emission features. Moreover, the extrapolation of intrinsic emission properties is generally made even more difficult by a contribution of bulk motion of material and relativistic particles to the overall energy production of the AGN.

We can therefore distinguish between three types of surveys (Hewett & Foltz 1994): the ones that intend to simply discover new objects, the ones that are designed to identify only the sources in a particular class without any completeness requirement and the surveys which have precise selection criteria and allow the selection probabilities to be inferred as functions of surveys' parameters. This last method is obviously the more difficult and useful for demographic and evolutionary studies.

A complete characterisation of the spectral energy distribution can then be provided only by the combination of data from different observations in several wavebands. Even the mere identification of the counterparts of a source in an another survey can often be very tricky. For example, the optical crosscheck of all the radio sources in the 3CR survey required over 30 years to be completed.

In the following, after briefly recalling the principal identification techniques in each waveband, we will focus on the description of the largest database of optical-UV quasar spectra as of today, given by the Sloan Digital Sky Survey (SDSS). We will then present the current fitting machinery for those spectra. To improve virial BH mass measurements and trying to unveil the evidence of quasar feedback driven by radiation pressure, it appears to be fundamental a more accurate approach to broad line fitting. We will therefore describe our new approach to QSO spectral fitting and the results we get from a large sample of SDSS-DR10 sources.

## 3.2 AGN surveys

It is to be remarked that, from an historical point of view, the first large AGN identification campaigns derived from the identification of, so to say, specific features in non-specific surveys. For example, the discovery of quasars itself by Baade & Minkowski (1954) has to be ascribed to the recognition of optical point-like counterparts to radio sources with a redshifted non-stellar spectrum (Schmidt 1963; Greenstein 1963; Schmidt & Matthews 1964). Similarly, Arp (1968) and Sargent (1970) consolidated a first procedure for AGN identification: a spectroscopic follow up characterization of compact blue galaxies previously detected (in the Markarian and Zwicky surveys respectively). Typical specific marks are (besides obviously broad emission lines) high ionization C, N, and O lines and a non-stellar Fe complex of low ionization lines. Anyway, a large population of highly obscured AGN found in radio and hard X-ray surveys do not show such features, therefore the use of the spectral energy distribution as an AGN indicator is not always a *passpartout*. In other words, the identification is intrinsically connected with selection effects and the surveys themselves by definition pick up objects with peculiar emission properties which are never ubiquitous in the vast variety of active galaxies.

### 3.2.1 Radio selection

As mentioned above, the radio waveband was the first in chronological order to be used to identify active galaxies. The undeniable advantages of the radio band surveys are the high sensitivity and position precision achievable (e.g.  $45''$  for the NRAO VLA Sky Survey and  $\sim 5''$  for FIRST). Moreover, almost all luminous compact radio sources with flat spectrum in the radio range are AGN. Only a little contamination by star-forming regions is encountered for low luminosity sources. Moreover, radio selection can also be possible through a morphological analysis, for every compact radio source showing double radio lobes or collimated jets hosts an AGN.

On the other hand, the selection effects is almost brutal: only  $\sim 10\%$  of the AGN appear to be radio-loud (White et al. 2000) and, in addition, the radio-selected AGN often do not show